New Jersey Institute of Technology

Digital Commons @ NJIT

Summer 8-31-2005

Emissivity of patterned silicon wafers in rapid thermal processing

Markus Rabus
New Jersey Institute of Technology

Follow this and additional works at: https://digitalcommons.njit.edu/theses

Part of the Other Physics Commons

Recommended Citation

ABSTRACT

EMISSIVITY OF PATTERNED SILICON WAFERS
IN RAPID THERMAL PROCESSING

by
Markus Rabus

The influence of patterns on emissivity in silicon wafers in rapid thermal processing systems has been investigated. In this study, two experiments with layered and patterned silicon wafers were conducted. The main difference in the experiments is the way in which the temperature was controlled. The first experiment was performed under Open Loop Intensity Control (OLIC). For OLIC, no feedback from the wafer is returned. It is assumed that supplying a certain power level will lead to the desired temperature. The other experiment used the Closed Loop Intensity Control. In this case, a feedback, in the form of temperature deviation is used to adjust the temperature.

By using the Stefan-Boltzmann T^4-law, a heat balance equation describing the incoming and outgoing heat can be derived. This heat balance equation can be used to calculate the spatial temperature differences due to different emissivities of the various thin film layers of patterned wafers. A mathematical model was developed based on the heat balance equation. The mathematical model was verified with experiments. The model showed good agreement with the experiments.

EMISSIVITY OF PATTERNED SILICON WAFERS
IN RAPID THERMAL PROCESSING

by
Markus Rabus

A Thesis
Submitted to the Faculty of
New Jersey Institute of Technology
in Partial Fulfillment of the Requirements for the Degree of
Master of Science in Applied Physics

Federated Physics Department

August 2005

APPROVAL PAGE

EMISSIVITY OF PATTERNED SILICON WAFERS IN RAPID THERMAL PROCESSING

Markus Rabus

Dr. Anthony T. Fiory, Thesis Co-Advisor   Date
Research Professor of Physics, NJIT

Dr. Nuggehalli M. Ravindra, Thesis Co-Advisor   Date
Professor of Physics, NJIT

Dr. Dentcho Ivanov, Committee Member   Date
Director of Microelectronics Fabrication Center, NJIT

Dr. Sufian M. Abedrabbo, Committee Member   Date
Assistant Professor of Physics, University of Jordan

Dr. Lamine M. Dieng, Committee Member   Date
Assistant Professor of Physics, City University of New York

BIOGRAPHICAL SKETCH

Author: Markus Rabus

Degree: Master of Science

Date: August 2005

Undergraduate and Graduate Education:

- Master of Science in Physics,
  New Jersey Institute of Technology, Newark, NJ, 2005

- Diplom (FH) Wirtschaftsingenieurwesen,
  University of Applied Science, Kempten, Germany, 2003

Major: Applied Physics

To my beloved fiancée,
Eva García Díaz

ACKNOWLEDGMENT

TABLE OF CONTENTS

LIST OF TABLES

LIST OF FIGURES

CHAPTER 1

INTRODUCTION

Single wafer processing has replaced batch processing in the most advanced integrated circuit fabrication. Among the advantages of single wafer processing that are becoming more important are better wafer to wafer process controls, lower risk of process failure affecting large numbers of valuable wafers, and the possibility of clustering together consecutive process steps. As the device sizes shrink, reducing the thermal budget (temperature-time product) and increasing the uniformity of the process become issues that are very critical. Reducing the thermal budget minimizes dopant diffusion and interface degradation. A small thermal budget decreases the diffusion. The dopants diffuse a short distance within the semiconductor. This leads to shallow junction formation and the accompanying thermal energy is sufficient to activate the dopants. This requirement is the driving force for rapid thermal processing (RTP) systems. However, the tradeoff between dopant diffusion and damage removal places a severe limitation for the technique in the formation of ultra-shallow junctions. In RTP systems, a single wafer is heated at atmospheric or low pressure under isothermal conditions [1]. The single wafer batch allows a shorter exposure time and reduces the thermal budget. The physical principle in RTP is the energy transfer between a heat source and an object, the semiconductor wafer.

In general, RTP-systems consist of three major parts:

- a heat source and controller
- a chamber in which the wafer is processed

1

- temperature measurement instrumentation.

Rapid thermal processes are used for the following applications:

- Rapid thermal annealing (RTA) (Source/Drain Implant Annealing)

- Rapid thermal oxide growth (RTO) (dielectric gate oxide)

- Rapid thermal chemical vapor deposition (RTCVD) (Formation of refractory silicides and nitrides)

- Rapid thermal diffusion (solar cells, shallow and steep junctions)

One main requirement of RTP is a uniform temperature distribution of the wafer in the chamber. The temperature distribution across a wafer is mainly influenced by the heat source arrangement, the reflector, the wafer geometry, pattern on the wafer etc. Since the wafer is mainly heated and cooled by radiative heat transfer, the radiative properties of the wafer play an important role. These properties are the absorptance, α, transmittance, τ, reflectance, r, and emittance, ε. All quantities are material dependent functions of wavelength and temperature. The relation between α, τ and r is determined by the conservation of energy (Kirchhoff's rule) under conditions of macroscopic thermal equilibrium.

$$r(\lambda,T) + \tau(\lambda,T) + \alpha(\lambda,T) = 1. \tag{1.1}$$

For a black body, r = 0, τ = 0 and α = 1, i.e. a black body absorbs all incident radiation. All matter with a temperature different from 0 K emits radiation. The radiation emitted by a body at a finite temperature is called temperature radiation. A black body has an emittance of unity for a given temperature and wavelength and is hence the best radiator at this temperature and wavelength. The concept of emittance is used in many temperature measurement applications. The Kirchhoff radiation law relates the emissivity with the absorptance.

$$\alpha(\lambda,T) = \varepsilon(\lambda,T). \tag{1.2}$$

In a fabrication process, the wafer is patterned with multilayers of various semiconductors, dielectrics, metals, and silicides with complex surface topography. The presence of patterns can cause a spatial variation of radiative properties across the wafer, leading to preferential absorption and emission, thus leading to temperature non-uniformity [2]. Pattern-induced temperature non-uniformity can lead to stress related problems such as wafer slip, dislocations and wafer warpage. Temperature non-uniformity further leads to variation in junction depth or gate oxide thickness across the wafer and thus reduces the device yield in fabrication [1].

In this work, the influence of temperature non-uniformity due to variation of the optical properties of patterned wafers are considered in two dimensions and modeled to simulate their behavior. The following Chapter 2 treats the necessary theoretical background of radiation thermometry in relation to RTP. Based on this background, a two-dimensional (2D) model for temperature distribution of patterned wafers is developed. In Chapter 3, specific process modes used in the experiments for emissivity pattern are described. Chapter 3 is followed by the results and discussion in Chapter 4.

CHAPTER 2

THEORETICAL BACKGROUND

2.1 Radiation, Emissivity and Heat Conduction

All radiation consists of energy quantum, the photon. Radiation energy is expressed as a multiple of a smallest quantum of radiation energy, which depends on the frequency, ν, and the Planck constant ($h = 6.626 \times 10^{-34}$ Js).

$$E = h\upsilon .\qquad\qquad(2.1)$$

Due to this quantization of energy, radiation can be considered as a particle flux of photons. Photons are not particles in the classical sense, since they have zero rest mass.

When radiation impinges upon a medium from the vacuum, part of the radiation is reflected and part penetrates the medium. The penetrating part of the radiation is refracted with a change in direction, i.e., refraction. Refraction is characterized by the refractive index, $n(\lambda)$, which is a material constant for a determined wavelength. The refractive index is the ratio of the velocity of the radiation in vacuum, c_0, to the velocity of the radiation in the medium, c_m.

$$n(\lambda) = \frac{c_0}{c_m} .\qquad\qquad(2.2)$$

The velocity within the medium for a certain wavelength is generally smaller than in vacuum. Therefore, for most cases, $n(\lambda) > 1$. As radiation passes through a medium, a part of the radiation is absorbed and another part is transmitted. In general, all not absorbed power is transmitted. The absorption is characterized by the extinction coefficient $k(\lambda)$. These optical material constants are related to the electrical properties

4

(dielectric constant, ε) of a medium by the Maxwell relation $\left(n = \sqrt{\varepsilon}\right)$. Generally, the absorption process converts the radiation energy into heat energy. The heat energy determines the temperature of a medium. Supply of heat energy increases the temperature and removal of heat energy decreases the temperature. The heat energy is derived by considering the bound atoms and molecules in a solid. These atoms and molecules can conduct small vibrations, called lattice vibrations. These vibrations are quantized like the optical radiation. The lattice vibrational quantum is called phonon. Phonons and electrons are treated to be in thermal equilibrium.

Other radiative properties of materials are transmittance, τ, reflectance, ρ, and absorptance, α. These quantities depend on wavelength and temperature and are related to $n(\lambda)$ and $k(\lambda)$. Transmittance is the ratio of the incident radiative intensity (I_0) to the intensity of the radiation exiting through the object (I_t).

$$\tau(\lambda, T) = \frac{I_t(\lambda, T)}{I_0(\lambda, T)}. \tag{2.3}$$

In the simplified case, we treat the radiation as incident perpendicular to the surface. The values of τ lie between 0 and 1. A transmittance of 1 implies that all radiation is transmitted, whereas $\tau = 0$ means that all radiation is reflected or absorbed. For perpendicular incidence, there is no difference between parallel and tangential components and the transmissivity can be calculated using:

$$\tau(\lambda, T) = \frac{4n^2(\lambda, T)k^2(\lambda, T)}{\left(n(\lambda, T) + 1\right)^2 + k^2(\lambda, T)} = e^{-\frac{a(\lambda, T)l_w}{\lambda}}, \tag{2.4}$$

where, $a(\lambda)$ is the absorption coefficient and is related to the extinction coefficient $k(\lambda, T)$ according to:

$$a(\lambda,T) = \frac{4\pi k(\lambda,T)}{\lambda}, \tag{2.5}$$

and, where, t_w is the thickness of the medium.

Reflectance is the relation between incident light (I_0) and the reflected light (I_r).

$$r(\lambda,T) = \frac{I_r(\lambda,T)}{I_0(\lambda,T)} \tag{2.6}$$

The relation between the refraction index, extinction coefficient and reflectivity at perpendicular incident is given by:

$$r(\lambda,T) = \frac{(n(\lambda,T)-1)^2 + k(\lambda,T)^2}{(n(\lambda,T)+1)^2 + k(\lambda,T)^2} \tag{2.7}$$

The remaining intensity, (I_a), is due to the absorbed energy by the medium. The absorptance is thus the ratio of absorbed intensity (I_a) to incident intensity (I_0):

$$\alpha(\lambda,T) = \frac{I_a}{I_0} \tag{2.8}$$

Due to the conservation of energy, the transmitted, I_t, reflected, I_r, and absorbed, I_a, intensities must sum up to the incident intensity, I_0.

$$I_t + I_r + I_a = I_0. \tag{2.9}$$

Equation 1.1 can be derived by dividing Equation 2.9 by the incident intensity, I_0. The absorptivity can be calculated using Beer's law:

$$I_a = I_0 e^{-a(\lambda,T)x}, \tag{2.10}$$

and knowing I_0 and I_a:

$$a(\lambda,T) = -\ln\left(\frac{I_a}{I_0}\right)x. \tag{2.11}$$

In Equation 2.11, x is the depth of penetration. The absorptivity is related with the extinction coefficient by Equation 2.5. For a black body, the absorption is 1. A black body is an ideal body which absorbs all the impinging radiation energy without reflection and transmission. For an opaque material, $\tau = 0$, in which case Equation (1.1) reduces to $r(\lambda,T) + \alpha(\lambda,T) = 1$.

Heat energy can be transported by radiation, conduction and flow (convection). The nature of heat radiation is electromagnetic. This electromagnetic radiation allows a body to release heat into vacuum. This release depends on the temperature and emissive properties of the body. It is important that, due to the energy balance, the environment also radiates emission back onto the body. Heat conduction is only possible in matter and is independent of a macroscopic movement of particles. For heat conduction, local differences in molecular energy resulting in temperature gradient are necessary. The transport of heat tries to equilibrate this temperature gradient. This lead to a change in the temperature distribution with time and it is called a non-stationary problem. A stationary problem, i.e. time independent, is only possible if there are heat energy sources to maintain the heat flow. Then a stationary temperature distribution will be established [3].

Heat transfer takes place whenever there is a temperature gradient in a medium. The values of temperature at all points of the medium of interest are called temperature distribution. An unsteady or transient temperature distribution is one in which temperature not only varies from point to point but also with time. A temperature distribution fluctuating in three dimensions is represented as $T = T(\vec{r},t)$. A steady state temperature distribution is one in which the temperature at a given point is time independent; it is a function of space coordinates only. The steady temperature

distribution is $T = T(\vec{r})$. The derivative with respect to time for a steady temperature

distribution is zero $\frac{\partial T}{\partial t} = 0$. The heat flux $\vec{q}$ is the heat transferred per unit time per unit

area and is proportional to the gradient of the temperature:

$$\vec{q} = -\lambda(T)\vec{\nabla}T \qquad (2.12)$$

λ(T) is the thermal conductivity. It is determined by:

$$\lambda(T) = \frac{(\dot{Q}/A)L}{T_1 - T_2}, \qquad (2.13)$$

where, ($\dot{Q}$/A) is the heat transported per unit area, and T_1 and T_2 are the temperature at

points separated by the distance L. The unit of heat flux is W/m^2 and for thermal

conductivity, the unit is W/mK [4]. The thermal conductivity is a thermo-physical

property. It can be interpreted as being equal to the heat transfer rate across a unit area

through a unit thickness for a unit temperature difference. Thermal conductivity of a

material depends on its chemical composition, physical structure and phase. It also

depends on the temperature and pressure to which the material is subjected. For

materials, however, thermal conductivity is much less dependent on pressure than on

temperature, so that the dependence on pressure may be neglected. Heat conduction in

solids with crystalline structures depends on the energy transfer by molecular and lattice

vibrations and free electrons. In general, the energy transfer by molecular and lattice

vibrations is not as large as by electron transport in conductors and semiconductors at

high temperature. Equation 2.12 can be interpreted as stating that if there is a negative

temperature gradient $\vec{\nabla}T$ at the considered point, then there will be a heat flux. The

minus sign in Equation 2.13 is necessary in order to meet the requirement of the second

law of thermodynamics that heat must flow from a higher to a lower temperature. That is, if the temperature gradient is negative then the heat flux is positive, and if, on the other hand, the gradient happens to be positive then the heat flux is negative. Therefore, $\vec{q}$ is a vector pointing in the direction of decreasing temperature normal to the isothermal surface passing through the point of consideration. Heat is transferred by conduction in the direction normal to isothermal surfaces from the higher temperature to the lower one.

All matter with a temperature different from zero emits radiation. This radiation is therefore called temperature or heat radiation. Heat radiation is energy transfer in the form of electromagnetic waves. A black body emits at a given temperature the maximum amount of radiation. The emissivity of a black body is therefore unity. The emissivity is equal to the absorptance α for all bodies at given temperature and wavelength. From Equation 1.2, Kirchhoff's radiation law can be derived. The radiation flux from any body is equal to the one of a black body multiplied by the emissivity:

$$\phi = \varepsilon \phi_S ,$$ (2.14)

where, ϕ_S is the radiant flux of a black body. The power radiated from a body by virtue of its temperature is proportional to the area and the fourth power of the body temperature. The proportionality coefficient is called Stefan-Boltzmann constant

$$\left(\sigma = \frac{2\pi^5 k^4}{15 h^3 c^2} = 5.67051 \cdot 10^{-8} \frac{W}{m^2 K^4} \right)$$

and the formula expressing the relation is called Stefan-Boltzmann law $P = \sigma \varepsilon A T^4$.

Real bodies (surfaces) do not meet the specifications of a blackbody, but emit radiation at a lower intensity than a black body of the same size, shape, and temperature. Let q^r and $q_b{}^r$ denote the radiation flux, (i.e. radiation emitted per unit surface area per

unit time) from a real and a black surface of the same temperature, respectively. Then, the emissivity, ε, of a real surface is defined as:

$$\varepsilon = \frac{q^r}{q_b^r}$$

(2.20)

In most cases, the emissivity is between 0.1 and 1. The emissivity of materials is a function of the optical properties of the starting wafer material (intrinsic emissivity), the layers on top of or buried in the wafer (extrinsic emissivity) and the specific optical properties of the reflective chamber with all components inside (effective emissivity). The power spans all wavelengths contained in the radiation, i.e. the whole radiated spectrum. The power of the radiation for a smaller region can be calculated by using the Planck radiation law. This law describes the radiation power of a black body as function of temperature T and wavelength λ:

$$dP(\lambda, T) = \frac{2\pi h c_0^2}{\lambda^5} \frac{1}{e^{hc_0/(k\lambda T)} - 1} d\lambda$$

(2.21)

The total radiated power, P, is obtained by integrating Equation 2.21 over the entire wavelength range from 0 to ∞. The radiated power increases with increasing temperature. The maximum in the Planck function occurs at $\lambda_{max} = \left[(hc_0)/(4.965kT) \right]$, which is known as Wien's displacement law. As temperature increases, the fraction of shorter wavelength increases. Therefore, it is possible to use the color impression of the whole radiation to determine the temperature of the radiation area. Temperature measuring instruments based on this radiation principle are called radiation pyrometers.

Above 600 °C, a bare silicon wafer will behave as an opaque grey body with ε = 0.7 over the entire wavelength range. Below this temperature, silicon behaves as a transparent non-grey body. The intrinsic emissivity value depends not only on the

roughness of the wafer surface and on the dopant concentration used, but also on the surface temperature and on the wavelength of the absorbed and emitted radiation. Electronic valence-to-conduction-band absorption is efficient for wavelength below the silicon bandgap of 1.2 μm. Above 6 μm, the absorption becomes efficient due to lattice vibrations. However, in the 1.2 μm $-$ 6 μm wavelength range and below 600 °C, the main heat absorption mechanism is by intrinsic free-carrier absorption. Thus, in this range, the emissivity is a strong function of the free-carrier density, and therefore, depends on the thickness, dopant concentration, and the temperature of the wafer [5].

2.2 Rapid Thermal Processing Systems

As mentioned in the introduction, RTP systems consist in general of three major parts (heat source, chamber and measurement instrumentation). In this section, RTP systems and methods are described in detail.

The main goal for the heat source is to achieve a short-time, high-temperature, isothermal wafer processing. Heat source can be divided into two major groups. The wafer can be either heated by transient radiation source such as arc lamps and tungsten-halogen lamps or by a continuous heat source. In the latter case, the wafer is moved rapidly in and out of the vicinity of the heat source and is often referred as a furnace system. The processing of the wafer follows a temperature versus time curve, T(t), determined by a recipe. This curve shows the temperature variation with time. The area under this curve is the thermal budget $\left(= \int T(t)dt\right)$.

The recipe determines the diffusion, sheet resistance and defect formation. The T-t curve is generally divided into three parts. The first part is called ramp-up. At the beginning, the wafer is brought from ambient temperature to a temperature below the activation energy. Then the wafer is further heated to the processing temperature at which the actual process takes place. For annealing, the temperature is high enough to activate the dopants and reduce defects. During implantation, the dopants occupy mostly interstitial impurity positions and are electrically inactive. Therefore, the wafer is heated and the dopant can diffuse to substitutional lattice sites. This process is known as dopant activation or annealing. In order to obtain a shallow junction, it is important that the time of diffusion is short such that the dopants do not diffuse beyond the desired active region. In case of oxidation, silicidation and nitridation, the temperature is at a level where respective formation takes place. In silicidation and nitridation, a precursor gas is additionally supplied.

The duration of the processing specifies whether it is a spike, impulse or flash process. The time scale for a spike, impulse and flash are of the order of 1 s, 0.1 s and 1 ms, respectively. At the end of the ramp-up, the areas with different absorptivity and emissivity will reach temperature different from the set point. For an activated process, this leads to process non-uniformity. During the cool down period, the wafer temperature is reduced mainly by emitting radiation to a cooler environment and is therefore characterized by the emissivity of the wafer. The transition from heating to cooling is limited by the thermal time constant of the wafer and the time constant of the heat source.

The wafer thermal response time thus determines the turn around time. Rapid cooling can quench point defects in a silicon wafer. Extending the duration for the steady state period will enhance the stationary temperature uniformity. Another important parameter is the ramp-up. Fast ramp would reduce thermal exposure of the wafers and reduce cost of ownership through reduced cycle time. Faster heating up will raise the temperature transient non-uniformity. This is due to the higher energy flux required during ramping up and should increase with faster ramp rates. Areas which are rapidly heated during the ramp-up will cool down faster. Areas which are heated more slowly will take a longer time.

The chamber design depends on the heat source. RTP systems employ two different types of chamber designs, namely cold wall and hot wall. The chamber is often interfaced with a gas handling system to provide a controlled ambient to form silicides, nitrides and oxides, or inert ambient annealing. In systems using a transient heater, the chamber is normally highly reflective and water cooled. The cold wall reactor is made from water-cooled metals such as stainless steel, aluminum, or other alloys in cylindrical or rectangular shapes. Reflectivity is accomplished by electro polishing the metal, or by coating it with reflective materials such as gold or aluminum [1].

In a lamp system, the reactor wall is typically not in thermal equilibrium with the objects within the chamber. The chamber top face is an air or water cooled quartz window plate that transmits the optical flux into the chamber. The cold walls have the advantage of minimal thermal memory effects that could further complicate temperature measurement. The continuous heating source system has a hot wall chamber. In this system, the convective and conductive heat flow plays the dominant role. The processing

chamber is made of quartz, silicon carbide, stainless steel, or aluminum with quartz windows. The chamber is normally a single wafer batch design, which optimizes the thermal budget.

The temperature distribution across a wafer is the consequence of a complex interaction of influences such as the heating source arrangement, the reflector, the wafer geometry, patterns on the wafer surface, etc. The arrangement of the heating source and all reflecting and absorbing parts which may influence the light flux onto the wafer comprise the optical design of an RTP system. Any optical concept can be characterized by three contributions of the light flux to the wafer surface:

   i.   light from the lamp (primary light) including multiple reflections

   ii.   heat radiation emitted from the wafer (secondary light) which is reabsorbed after single or multiple reflections.

   iii.   passive components, quartz, wafer support structure, window, guard rings.

Contribution (i) is the active component which is controlled in order to achieve the desired temperature-time cycle. Its absolute value depends on the ramp rate and the temperature. Contributions (ii) and (iii) are passive because the emission of heat radiation is a consequence of the surface temperature. It may alternatively be regarded as component which reduces the net energy loss (the higher the reabsorbed heat radiation the lower the energy loss). During a flux equilibrium (also denoted as stationary state), the energy loss of the wafer is balanced by the absorption of light. Ramping (cooling) is achieved by an excess (deficit) of the absorbed energy over the energy loss – the larger the energy excess (deficit) the larger the ramp (cooling) rate [7].

RTCVD is a process in which thin film layers are deposited on a substrate by using rapid thermal processing. One of the principal advantages of RTCVD is that sharp transitions are obtained between layers of differing composition or doping, while exposing the substrate to a much lower thermal budget than a normal low-pressure chemical vapor deposition (LPCVD) process. Moreover, RTCVD can be a cold wall system which generates less particulate contamination. It also reduces problems of auto doping and interdiffusion through a lower thermal budget than LPCVD [8].
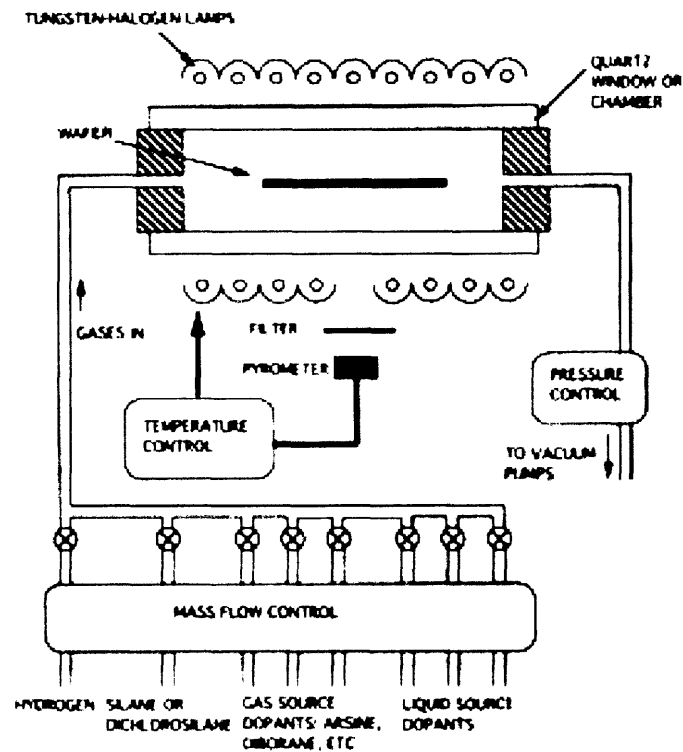
Figure 2.1 Schematic of a RTCVD system [8].

RTA is of critical importance in electrical activation of dopants and damage annealing. After dopants are implanted, these dopants are at interstitial lattice sites, which are electrically neutral sites. Hence the dopants have to be activated. The dopants get activated by diffusion to substitutional lattice sites. During the activation of implanted

dopants, also diffusion out of the active region occurs, which is highly undesirable when shallow junctions are expected. The goal in junction formation is to achieve a low sheet resistance with a high concentration of electrically active dopants and with as little dopant diffusion as necessary [8].

A spike-annealing technique was introduced to control dopant diffusion in shallow junction formation and is integrated with contact junction and gate electrode activation. Current spike annealing methods use infrared heating that is characterized by near thermal equilibrium across the thickness of the wafer. The variables are heating rates, the switching time from heating to cooling, and the cooling rate. In spike annealing, the intent is to limit the undesired diffusion out of the active region, while at the same time reaching the peak temperature required for dopant activation. This is achieved by heating to the desired temperature in minimum possible time and cooling down immediately without any dwell time at the peak temperature [8].

Flash annealing (Figure 2.2) [8] uses a high optical flux for faster heating to either briefly melt the wafer surface or selectively raise the surface temperature. Upon termination of the light pulse, the surface temperature rapidly cools down by thermal diffusion into the bulk of Si. However, this rapid cooling may cause problems like residual lattice defects and dopant metastability.
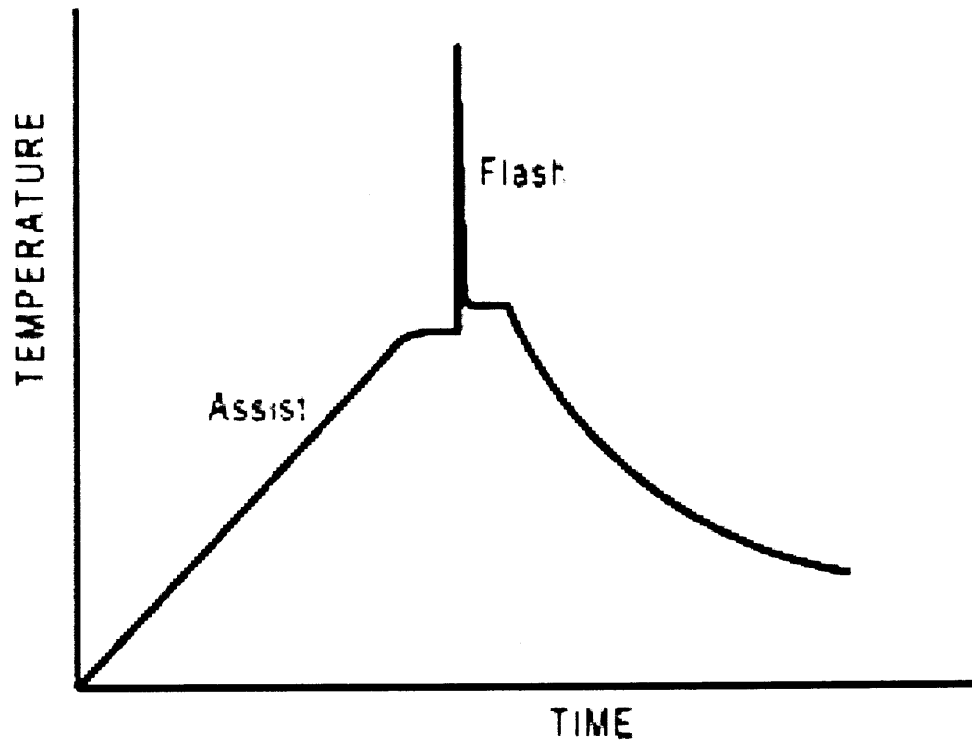
Figure 2.2 Wafer surface temperature versus time for flash annealing process [8].

2.1.1 Furnace System

In a furnace system, a temperature gradient is realized within the reactor, i.e. the heating power is constant and the wafer temperature is determined by the position as in Figure 2.3 [9], which shows a schematic of a heated bell jar. In this system, the wafer is heated from both sides.
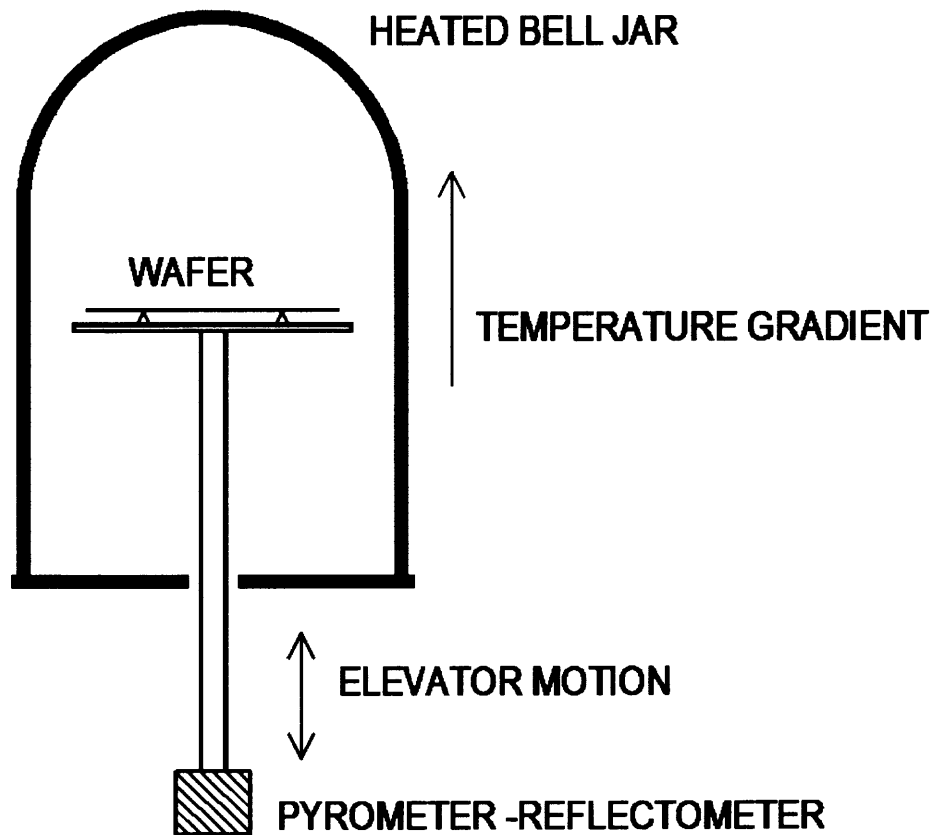
Figure 2.3 Schematic of a continuous heat source system, furnace process [9].

The spectral temperature at the top of the bell jar is approximately 200 °C to 400 °C above the RTP process temperature. Figure 2.4 [10] shows an example of a vertical furnace system from Axcelis. Another possible furnace method is to feed the wafer horizontally.

Figure 2.4 Furnace RTP system from Axcelis [10].

The furnace system is an inertial system and has limited operation speed. Figure 2.5 [9] shows that the processing time is in the range of seconds. At the beginning, the wafer is brought into the furnace to a pre-heat stabilization temperature near 750 °C. After nearly one minute, the heating increases rapidly to the processing temperature, 1075 °C, and is then cooled to 750 °C, after which the wafer is withdrawn from the furnace. The crucial part of the temperature cycle is when the temperature exceeds the dotted line in Figure 2.5 [9], which represents the activation of the dopants, formation of oxides, silicides or nitrides. The process depicted in Figure 2.5 is for an implant anneal. The dotted line corresponds to the part of the cycle that is dominant in activation of the dopants. An example of low temperature spike process is Ni silicidation. The spike is around 350 °C to 400 °C.
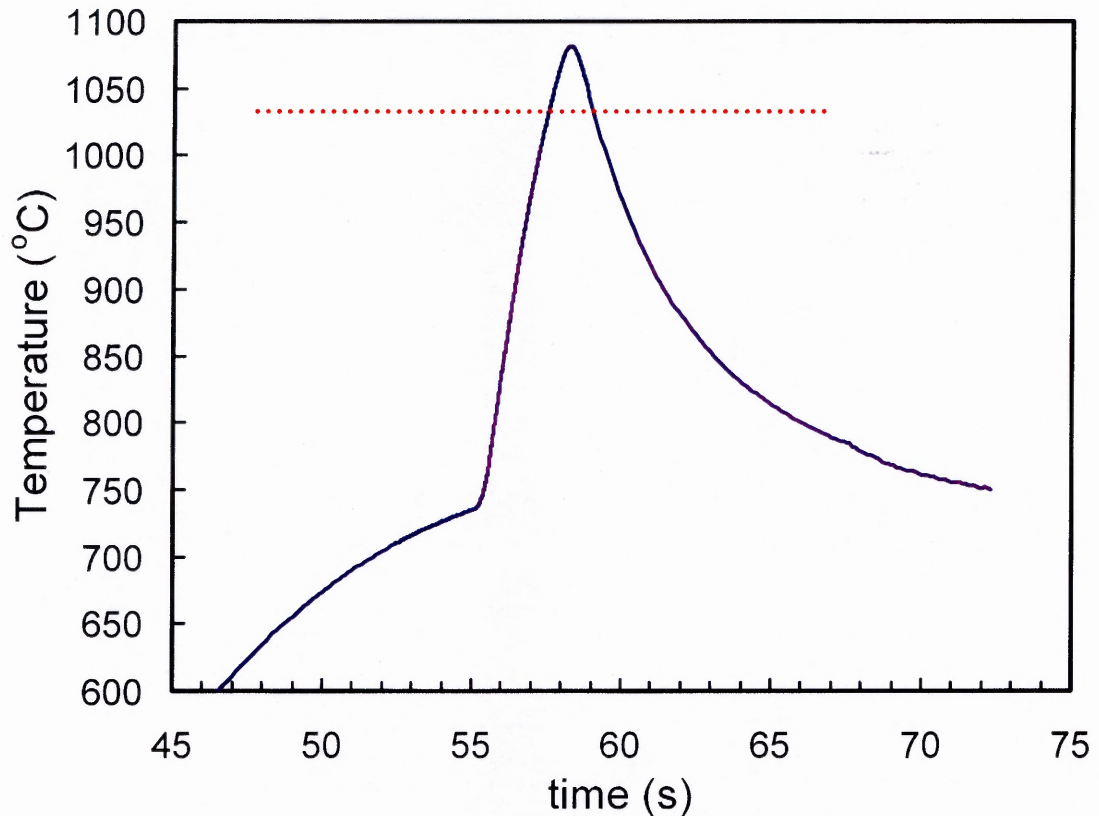
Figure 2.5 Wafer surface temperature versus time of a spike anneal process furnace system [9].

2.1.2 Lamp Systems

Heating lamp arrays are used to irradiate the wafer either from one side or from both sides. In the lamp system, the power input of the lamps determines the wafer temperature. Power control operates under the assumption that if the same power is delivered to the lamps, the same intensity will be emitted. Thus, if the wafer and process chamber conditions do not vary, then the absorbed intensity will be reproducible. The issues with power control are chamber window and wall hazing altering the absorption and reflection properties of the wafer environment, lamp aging, wafer variations, and line voltage regulation [11].
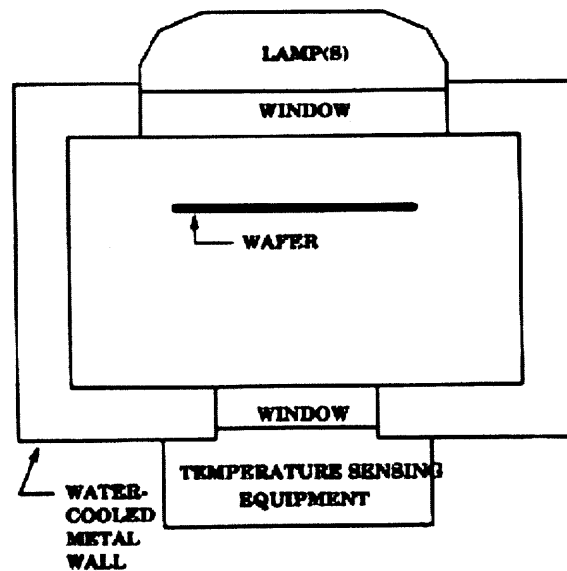
Figure 2.6 Schematic of a single sided lamp RTP system [8].

As can be seen in Figure 2.6 [8], in a lamp system, the lamps for single sided heating are on top and opposite of the temperature measuring equipment, which looks from the bottom unto the wafer. In this system, there is also the possibility to cool the walls. Lamps and temperature measurement subsystems are separated from the chamber by a window, i.e., mainly quartz. Problems resulting from this arrangement, wafer between lamps and temperature sensors, and from the windows will be discussed later.

Lamp systems allow further advantages like pulsing the lamps and flash RTP. There are different types of lamps. These are the incandescent tungsten-halogen lamps and the arc-lamps. The difference between the two is in the wavelength of radiation. Arc lamps operate in the wavelength range of 0.2 to 1.4 μm. Most RTPs utilize tungsten halogen lamps as the heat source. The tungsten lamp spectrum is in the wavelength range of 0.3 – 4 μm, making it a source of interference for pyrometers operating in this regime. Filters and chamber design have been developed to minimize this effect.
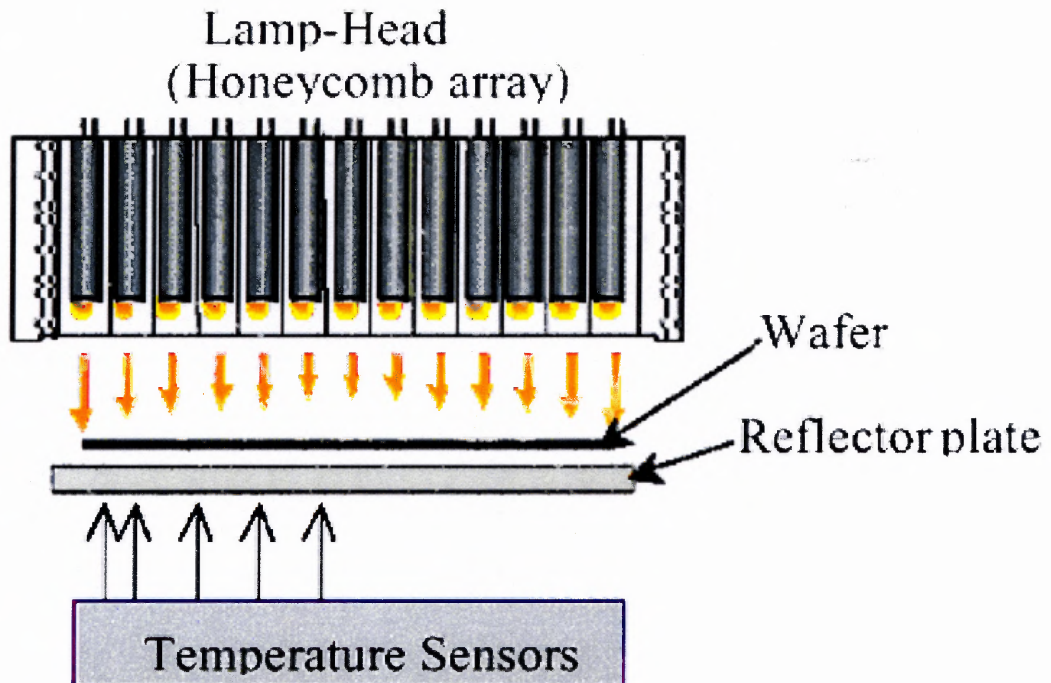
Figure 2.7 Schematic of the honeycomb array lamp system from Applied Materials [12].

Figures 2.7 [12] and 2.8 [12] illustrate the incandescent lamps system manufactured by Applied Materials. Incandescent lamps have a thermal time constant of > 0.1 s and therefore allow only spike or longer duration processes. The lamps are ordered like a honeycomb and separated from the wafer with a quartz window, as can be seen in Figure 2.7. The honeycomb array allows actuating each lamp or a cluster of lamps in independent zones, which gives more freedom in controlling the wafer temperature distribution.
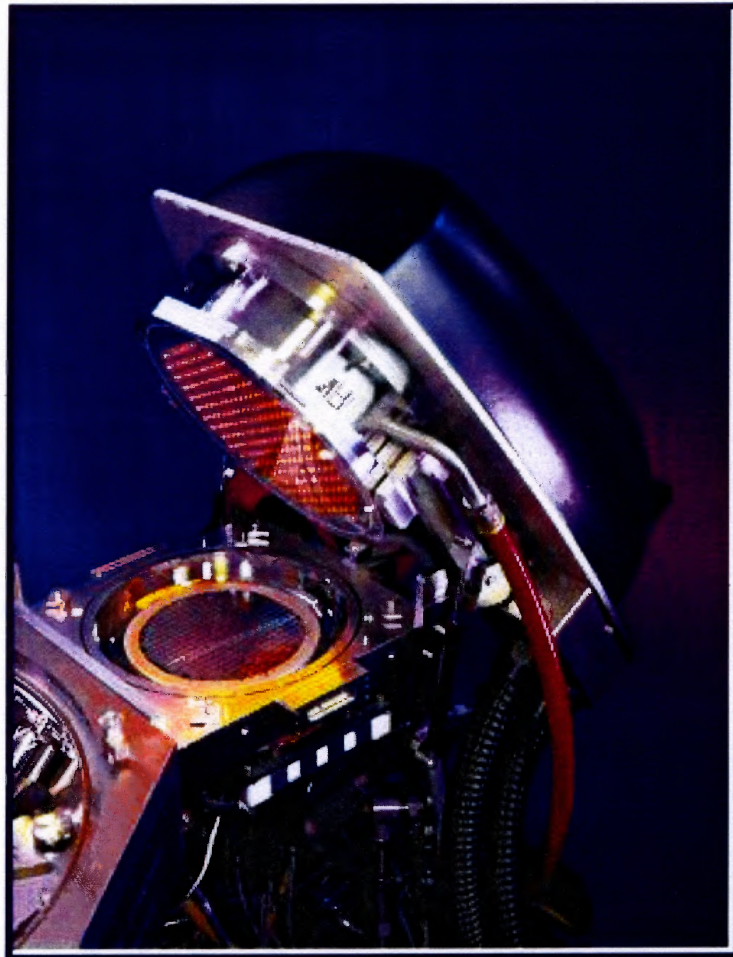
Figure 2.8 Incandescent lamp system from Applied Materials [12].

As can be seen in Figure 2.9 [9], the spike process for a lamp system looks very similar to that of a constant power heat source. The wafer is pre-heated to a temperature of 650 °C and is held there for a short period. Afterwards, the wafer is brought very rapidly to the processing temperature of approximately 1000 °C by increasing the power of the lamp system. After heating the wafer to 1050 °C, the lamps are turned off and the wafer cools down to a wafer handling temperature of about 650 °C.
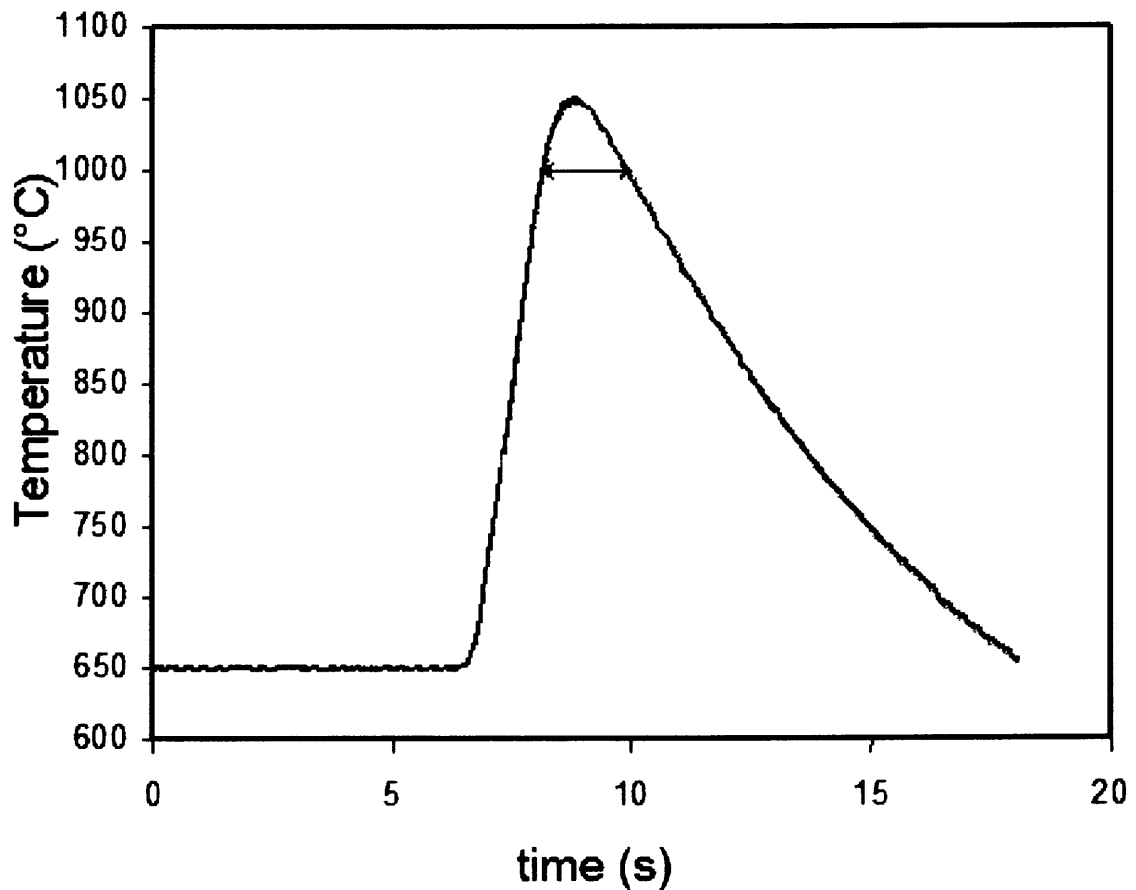
Figure 2.9 Wafer surface temperature versus time graph for a lamp spike process [9].

The higher temperature is due to heating and cooling rates characteristic of the lamp system. The incandescent lamps have an afterglow. This heats the wafer above 1000 °C.

The soak at 650 °C (lamp) or 750 °C (furnace) allows the temperature of silicon wafer to equilibrate, owing to the strong temperature dependence of the IR absorption of silicon at low temperature. The reason to hold the wafer at a certain temperature is that most lamp systems operate in the IR wavelength range. The temperature dependence of the silicon bandgap is given by:

$$E_g(T) = E_g(0) - \frac{\alpha T^2}{T + \beta}, \qquad (2.22)$$

where, α and β are fitting parameters and T is the temperature in Kelvin. For silicon, the

values of these parameters are:

$$\alpha = 0.473 \text{ meV/K}$$

$$\beta = 636 \text{ K and}$$

$$E_g(0) = 1.166 \text{ eV } [13]$$

From Equation 2.22, it can be seen that, with increasing temperature, the bandgap

of silicon decreases. With the knowledge of the bandgap, the wavelength of photons at

which the semiconductor starts to absorb radiation can be calculated using the following

equation:

$$\lambda = \frac{1240}{E_g}.$$ (2.23)

If E_g is in eV, then λ is obtained in nm [14]. For silicon, at room temperature, the

absorption process starts at 1.106 μm which lies near to the short wavelength end of the

infrared region. At wavelength shorter than 1.106 μm, the energy is dissipated in the

material in the form of heat. Comparing this with the spectral range of tungsten halogen

and arc lamps, it can be seen that the arc lamps are more effective than the tungsten

halogen lamps. Most lamp systems are mainly infrared sources. This absorbed radiation

is only a small fraction of the infrared range and therefore the wafer heats very slowly.

This is the reason for the wafer to be held for a longer time at a certain temperature. As

temperature increases, the fraction of absorbed infrared radiation gets bigger. Figure 2.10,

based on Equation (2.22), shows the temperature dependence of the bandgap for intrinsic

Si. It clearly illustrates the decreasing bandgap of silicon with increasing temperature.

Temperature dependence of the bandgap of Si
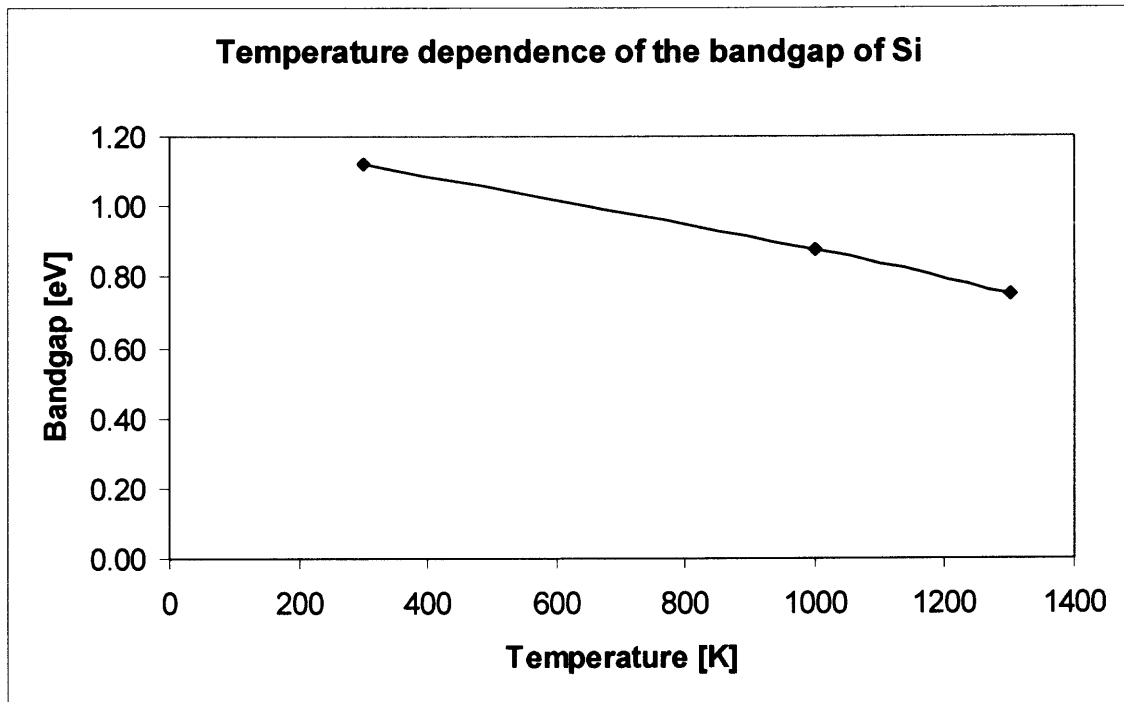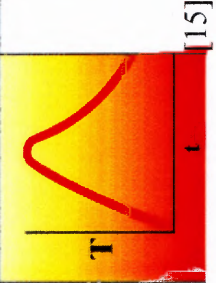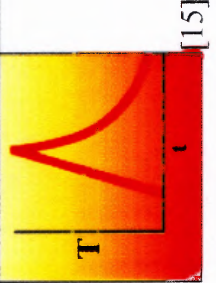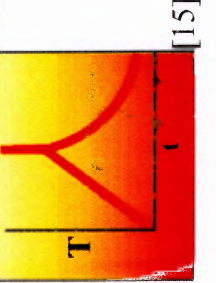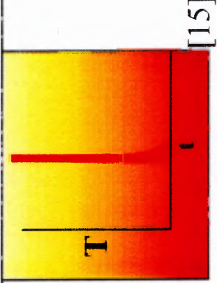
Figure 2.10 Bandgap for Si at 300, 1000 and 1300 K.

Above the cutoff wavelength for band-to-band transitions, silicon can still absorb photons, but, through a different mechanism called free carrier absorption. In this regime, by absorbing the energy of photons, free carriers can make transitions to higher energy levels in the same valley. Clearly, the transition requires momentum change which can be provided by phonons or ionized impurity scattering. Naturally, the amount of free carrier absorption in the wafer is proportional to the number of free carriers which is determined by the doping level of the substrate and the process temperature. In silicon, free carrier absorption occurs at wavelengths above 2μm. Therefore considerable amount of free carrier absorption takes place when tungsten halogen lamps are used for heating the wafer [11].

A further enhancement in process efficiency is the impulse RTP system. In impulse RTP systems, the thermal budget is further increased. A producer of impulse RTP systems is DaiNippon Screen. Their RTP system uses Xe-lamps as heat source. The processing time is only 10 ms and therefore the time in which the diffusion takes place is very short. This makes shallow junctions possible. The doping profile stays mainly the same and the deviation from the profile is only small. The dopants do not diffuse very far.

The flash anneal recipe is created from the standard implant anneal recipe by shortening the steady state to 1 second while keeping the ramp rates the same. In order to maintain the temperature sensitivity of the implant anneal, the temperature set point of the flash recipe has to be increased. The process time is further shortened. Table 2.1 gives an overview of the different processes.

Table 2.1 Overview of the Different Process Modes

Process	Advantages	Disadvantages	Time vs Temperature	Applications
Spike process	Broad applications.	No shallow junction; High outdiffusion of dopants; Doping profile not attained.	[15]	Silicidation, nitridation, annealing, gate oxides.
Impulse process	Shallow junction formation.	Narrow applications.	[15]	Shallow junction formation.
Flash process	Ultra Shallow junction formation.	Narrow applications.	[15]	Ultra shallow junction formation.
Laser process	Ultra Shallow junction formations; Doping profile attained; Short melting.	Raster treatment.	[15]	Devices with sharp doping profile.

2.1.3 Temperature Measurement Equipment

Current RTP systems employ two classes of temperature sensors: thermoelectric detectors and photon (or quantum) detectors [5]. The mainly used thermoelectric detectors are the thermocouple and thermopile. A thermocouple is based on the Seebeck principle. A thermopile is a group of thermocouples connected in series.

The Seebeck effect converts a temperature difference into electricity by using the fact that the Fermi level of a conductor depends on temperature. In a pure electron conductor, the Fermi level is proportional to temperature; however, the Fermi level is material dependent. If two materials are connected, a voltage between the opposite ends of the materials can be measured. At the junction, the Fermi level of both materials are equal and hence no voltage can be measured. The Fermi level is proportional to the temperature and therefore the voltage scales with temperature.

A thermocouple consists of a junction of two bimetals. The mainly used bimetals junctions are Ni-Cr/Ni-Mn-Al and Pt-Rh alloy combinations. Thermocouples work in contact mode, i.e. heat conduction, as well as by non-contact absorption of infrared photons emitted by the hot object. A ceramic heat sink is an active detector. The ceramic supports a $1 - 3$ µm thin membrane of polyethylene terephtalate. On the hot junction area of this membrane, thin film structures are deposited. One side of the membrane area is blackened to increase the absorption efficiency. A material with high positive Seebeck Coefficient, α_s, for example, Sb, and as opposite pole, a material with negative α_s, for example, Bi, is used [5].

The disadvantages of thermocouples are the irreproducible thermal contact, the non-inert contact with the wafer, incompatibility with reactive gases and the degradation upon intense thermal cycling. The point of contact may act as a heat source or sink causing temperature variations across the wafer and may exhibit a memory effect from wafer to wafer. On the other hand, thermopile detectors are cheaper, more compact and more sensitive in a broad range of temperatures than photon detectors [5].

The radiation laws determine the basis for temperature measurement in photodetectors. They measure the radiation of a body in a mostly small range of wavelengths for which the temperature should be determined. Photodetectors utilize quantum phenomenon in which an infrared photon is absorbed by a semiconductor. Upon absorption, the photon creates an electron hole pair. The free carriers are then detected, which can be converted into IR intensity [5].

The radiance is comprised of three components; emission from the wafer, transmitted lamp irradiance, and reflected flux from the chamber, walls or shield. Once emissivity is known, wafer temperature can be calculated from Planck's equation. In general, the glowing body is not a black radiator, i.e., its absorptivity ε is smaller than 1. Therefore, the specific radiation is smaller than that of a black body at the same temperature. The real temperature is higher than that measured with the pyrometer, which is called the black temperature T' at the wavelength λ. The IR intensity is related to the Planck function. According to Kirchhoff's law, the specific radiation of the body at temperature T is given by:

$$R = R_S \varepsilon = \varepsilon \frac{8\pi h \upsilon^3}{c^3} e^{-\frac{h\upsilon}{kT}}$$

(2.24)

Wien's approximation can be used, because the measured frequencies are far right from the maximum. This specific radiation equals the radiation of the black body at temperature T'.

$$R = \varepsilon \frac{8\pi h\upsilon^3}{c^3} e^{-\frac{h\upsilon}{kT}} = \frac{8\pi h\upsilon^3}{c^3} e^{-\frac{h\upsilon}{kT'}}.$$ (2.25)

By taking the logarithm of this equation, the following equation can be derived:

$$\frac{1}{T} - \frac{1}{T'} = \frac{k}{h\upsilon} \ln \varepsilon = \frac{k}{hc} \lambda \ln \varepsilon$$ (2.26)

For $\varepsilon = 1$, T equals T' and for $\varepsilon < 1$, ln (ε) is smaller than 0 and therefore T > T' [4].

There are two groups of pyrometers, the single wavelength pyrometers and the multiple wavelength pyrometers. A pyrometer allows a contact less temperature measurement. Most RTP systems use pyrometers in the wavelength range of 0.95 μm – 10 μm. There are 0.95 μm, 2.6 μm – 3.5 μm, 2.7 μm, 4.5 μm – 5.0 μm, and 5.0 μm – 10 μm pyrometers available. They are capable of reading up to a resolution of ± 0.1 °C with a frequency greater than 20 Hz and a lifetime of 1 year. Photon detectors are more sensitive in narrower spectral ranges and have much shorter response time [5].

The bandgap of silicon is in the near infrared wavelength region. All radiation with a longer wavelength than that of the bandgap is transmitted. Most of the infrared radiation is therefore transmitted. This radiation influences the measurements performed by the pyrometer. Hence, often filters outside of the spectra emitted by the heat sources are used. These filters narrow the optical bands to circumvent the problems related to the transparency of silicon in the infrared wavelength range at low temperatures.

Another possibility to reduce the problem associated with the transparency of silicon is to use long wavelength detectors. Furthermore, long wavelength detectors reduce the oscillation frequency of the emissivity as a function of the thickness of the growing overlayers. A disadvantage of long wavelength detectors is the low signal to noise ratio of detection. Consequently, all reactor components should be kept cold, because these warm system components interfere with the detection of the wafer radiation. A rougher backside can scatter more reflected light into the pyrometer, and thus increase the effective emissivity. This problem may be suppressed by using a smaller pyrometer view angle or by making the chamber bottom less reflective [14].

Optical pyrometers need to be calibrated. The calibration of pyrometers in RTP systems are done at two distinct levels. First is a system level calibration, obtained by matching the pyrometer reading to that of a thermocouple in contact with a sacrificial reference wafer. Second is a wafer level calibration. If the emissivity is likely to show small variations for the individual wafer within a batch, a wafer level calibration is needed. Here, one measures the extrinsic emissivity directly by an *ex situ* reflectivity measurement prior to processing, or one measures the effective emissivity in situ before or during processing [5].

Table 2.2 Overview of Temperature Measurement Equipment

Temperature measurement device	Principle	Advantages	Disadvantages
Thermocouple	Seebeck effect converts temperature difference into voltage.	– Simple – Sensitive in a broad spectral range – Compact	– Non-inert contact with the wafer – Irreproducible contact – Degradation – Incompatibility with reactive gases
Photodetector	Photons create electron-hole pairs. Free carriers are detected.	– Sensitive in a narrow spectral range – Short response time	– Transparency of silicon, detection of heat source – Roughness can increase emissivity
Bolometer	Change in resistance with wavelength	– Simple – Sensitive in a broad spectral range	– Needs cooling to increase sensitivity to temperature changes

2.3 Multi-Rad Version 1.0 for Windows 95 and NT

2.3.1 Introduction to Multi-Rad

Multi-Rad was used to calculate the spectral properties. Therefore, an understanding of Multi-Rad is important. The following excerpts from the Multi-Rad manual are reproduced for completeness, reference and background [16].

Multi-Rad was developed at the Massachusetts Institute of Technology (MIT) by Jeffrey P. Hebb, Justine Cave, David Wang, Shwan MacFarland, and Klavs F. Jensen. Multi-Rad predicts radiative properties of layered materials by utilizing electromagnetic theory for multilayers. The basic theory is described by J. Hebb and K. F. Jensen in "The effect of multilayer patterns on temperature uniformity during rapid thermal processing", J. Electrochem. Soc. 143, 1142 – 1151 (1996) [2]. The basic research underlying this software was supported by SEMATECH and the Semiconductor Research Corporation.

SEMATECH sponsored the development of the Windows 95 based software under the direction of Tony Speranza.

Multi-Rad is a PC-based software that calculates radiative properties of thin film stacks, with emphasis on semiconductor applications. It runs on Windows 95 or Windows NT. At the heart of the calculation is thin film optics, implemented in the form of the matrix method of multilayers. This model assumes that the layers are optically smooth and parallel, and that the materials are optically isotropic (the optical constants are not dependent on crystallographic orientation). Therefore, the theory does not predict any variation of properties in the azimuthal direction. For a given multilayer stack at a prescribed temperature, the user can calculate the radiative properties as they vary with wavelength and angle of incidence.

2.3.2 Calculation Method used by Multi-Rad

The matrix method of multilayers predicts the reflectance and transmittance of a multilayer stack for a given wavelength and angle of incidence. Radiation at a given wavelength is treated as coherent and, therefore, interference effects are taken into account. The main assumptions of the theory are that the layers are parallel and optically isotropic, the surface is optically smooth, and the area in question is much larger than the wavelength of incident radiation, i.e., no edge effects. A generic layered structure is shown in Figure 2.11.
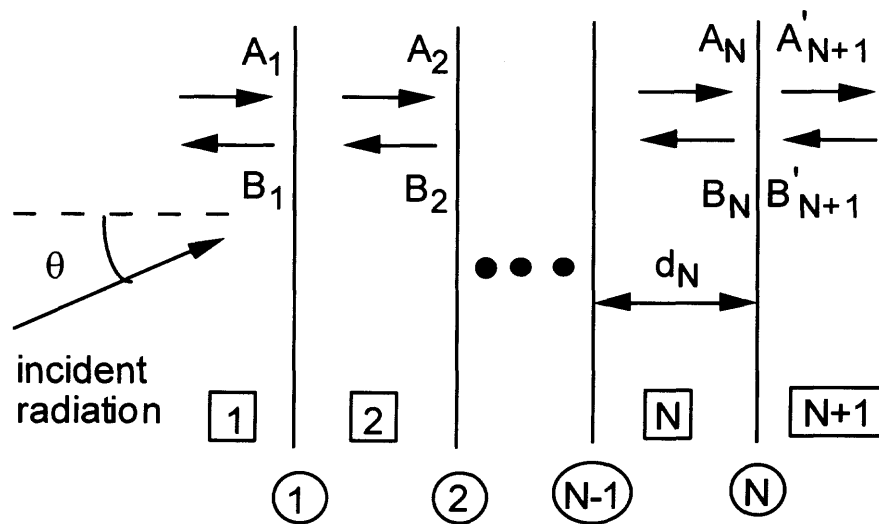
Figure 2.11 Notation for matrix method of multilayers.

There are N layer interfaces (circled) and N+1 layers (squared), including the unbounded transparent media on each side of the actual stack. A_i and B_i are the amplitudes of the forward and backward propagating electric field vectors on the left side of interface i. The prime notation on A'_{N+1} and B'_{N+1} indicates that these are the amplitudes on the right side of interface N. Light is incident on interface 1, with an angle of incidence θ_1.

The central equation of the multilayer theory relates the amplitudes on the left side of interface 1 with those on the right side of interface N:

$$\begin{bmatrix} A_1 \\ B_1 \end{bmatrix} = \left[\prod_{i=1}^{N} P_i D_i^{-1} D_{i+1} \right] \begin{bmatrix} A'_{N+1} \\ B'_{N+1} \end{bmatrix} = \begin{bmatrix} m_{11} & m_{12} \\ m_{21} & m_{22} \end{bmatrix} \begin{bmatrix} A'_{N+1} \\ B'_{N+1} \end{bmatrix} \tag{2.27}$$

where, P_i is the propagation matrix, D_i is the dynamical matrix, and m_{ij} is an element of the transfer function matrix. The propagation matrix accounts for the effect of absorption and interference within a layer i bounded by two interfaces. Because layer 1 is not bounded by two interfaces, the propagation matrix has no meaning, and P_1 is set equal to the identity matrix. For layers 2, 3, ... , N, the propagation matrix is:

$$P_i = \begin{bmatrix} e^{i\phi_i} & 0 \\ 0 & e^{-i\phi_i} \end{bmatrix} \qquad (2.28)$$

where, $\phi_i = \dfrac{2\pi \bar{n}_i d_i \cos\bar{\theta}_i}{\lambda}$ is the phase shift. The complex refractive index is $\bar{n}_i = n_i + i\kappa_i$,

where, n is the refractive index and κ is the extinction coefficient. It is assumed that the

bonding media are in vacuum, with a refractive index of 1. The thickness of the layer is d,

$\bar{\theta}_i$ is the complex angle, and λ is the wavelength of the incident wave in vacuum.

The dynamic matrix accounts for reflection and refraction at the interface i,

relating amplitudes of the reflected and refracted waves on either side of the interface.

Depending on the state of polarization of the wave, the dynamical matrix is given by:

$$D_i = \begin{bmatrix} 1 & 1 \\ \bar{n}_i \cos\bar{\theta}_i & -\bar{n}_i \cos\bar{\theta}_i \end{bmatrix} \quad \text{s wave} \qquad (2.29)$$

$$D_i = \begin{bmatrix} \cos\bar{\theta}_i & \cos\bar{\theta}_i \\ \bar{n}_i & -\bar{n}_i \end{bmatrix} \quad \text{p wave} \qquad (2.30)$$

where, s and p indicate that the electric filed vector is perpendicular and parallel to the

plane of incidence, respectively. Non-absorbing layers have purely real refractive indices,

so they have purely real angles that can be interpreted as the direction of propagation in

the layer. Absorbing layers have complex refractive indices, so they have complex angles

which have no direct physical interpretation. The angle θ_1 is purely real and interpreted as

the angle of incidence. Given the angle of incidence, the complex angles for the other

layers are calculated in succession using the complex form of Snell's law,

$$\sin\bar{\theta}_{i+1} = \frac{\bar{n}_i}{\bar{n}_{i+1}} \sin\bar{\theta}_i. \qquad (2.31)$$

The reflectance for an s or p wave for the complete stack is the ratio of the intensities of the forward and backward propagating waves on the left side of interface 1. The transmittance for an s or p wave is the ratio of the intensities of the forward propagating wave on the right side of interface N and the forward propagating wave on the left side of interface 1. The intensity of an electromagnetic wave is proportional to the square of its amplitude. Thus,

$$R_{s/p} = \frac{B_1}{A_1} = \left|\frac{m_{21}}{m_{11}}\right|^2 ,$$

$$T_{s/p} = \frac{\bar{n}_{i+N}\cos\bar{\theta}_{i+N}}{\bar{n}_1\cos\bar{\theta}_1}\frac{A'_{N+1}}{A_1} = \frac{\bar{n}_{i+N}\cos\bar{\theta}_{i+N}}{\bar{n}_1\cos\bar{\theta}_1}\left|\frac{m_{21}}{m_{11}}\right|^2 .$$

(2.32 a, b)

Thermal radiation is usually well approximated as unpolarized, in which case, the spectral directional reflectance and transmittance, $R_{\lambda,\theta}$ and $T_{\lambda,\theta}$, may be calculated as a simple arithmetic average of the s and p wave properties. When comparing calculated spectra to measured spectra, spectral averaging must be performed over a spectral interval $\Delta\lambda$, where $\Delta\lambda$ corresponds to the spectral resolution of the spectrometer or pyrometer used to perform the measurement. Implementing the theory this way makes it general in that predicted properties do not depend on classifying the radiation in a layer as coherent or incoherent.

The spectral directional absorptance is calculated by subtracting the reflectance and transmittance from unity, and the spectral directional emittance is calculated by assuming Kirchhoff's law on a spectral basis:

$$\alpha_{\lambda,\theta} = \varepsilon_{\lambda,\theta} = 1 - R_{\lambda,\theta} - T_{\lambda,\theta}$$

(2.33)

where, the subscripts λ and θ have been introduced to indicate spectral and directional properties, respectively. Kirchhoff's law on a spectral basis is valid if the emitting object

is in local thermodynamic equilibrium, i.e., it can be characterized by a single temperature. If there is a significant temperature gradient in the part of the wafer that is emitting, or if the phonons and electrons are not in thermal equilibrium (e.g. laser annealing), then Kirchhoff's law becomes invalid. For most RTP processes, neither of these conditions is encountered for a silicon wafer.

To obtain the hemispherical spectral properties, integration over all directions in the hemisphere is performed. The matrix method of multilayers described above makes the assumption that there is no variation of the radiative properties with azimuthal angle. The spectral absorptance integrated over a particular range of angle of incidence, defined by θ_{min} and θ_{max} is given by:

$$\alpha_\lambda = \frac{\int_{\theta_{min}}^{\theta_{max}} \alpha_{\lambda,\theta} \cos\theta \sin\theta \, d\theta}{\frac{1}{2}\left(\sin^2\theta_{max} - \sin^2\theta_{min}\right)} \tag{2.34}$$

where, θ is the angle of incidence. The expression is analogous for emittance, reflectance, and transmittance.

To calculate the total amount of energy that will be reflected, transmitted, emitted or absorbed in a certain spectral range, the spectral properties must be integrated with respect to wavelength for a certain black body distribution of energy. For example, the total absorptance in a band i is:

$$\alpha_i = \frac{1}{\sigma T_b^4 \phi_{T_s}^k} \int_{\lambda_1}^{\lambda_2} e_b(\lambda,T_b)\alpha_\lambda(\lambda)d\lambda \tag{2.35}$$

where, e_b is the Planck function evaluated at the black body source temperature T_b, λ_1 and λ_2 are the spectral bounds of the band i, $\phi_{T_s}^k$ is the fraction of the black body energy in the

spectral absorptance. The integral is analogous for emittance, transmittance, and reflectance.

A change in emittance of a multilayer stack at a given nominal temperature leads to pyrometric temperature measurement error. A rigorous calculation of this error must take into account the pyrometer, the associated optics, filters, and many other complicated factors which are beyond the scope of Multi-Rad. The software does, however, do a very simple calculation of this error to give an estimate of the impact of uncertainty in layer thicknesses on temperature measurement error. The following expression provides this estimation:

$$\Delta T = \frac{T_{nom}^2 \lambda}{14400} \frac{\Delta \varepsilon}{\varepsilon} \tag{2.36}$$

where, T_{nom} is the nominal wafer temperature that would be measured if the stack has the nominal emissivity, ε, $\Delta \varepsilon$ is the change in emissivity of the stack due to a change in the film thickness of one or more of the layers in the stack, and ΔT is the temperature measurement error incurred due to this emissivity change.

Spectral analysis method used to calculate the radiative properties is thin film optics, implemented in the form of matrix method of multilayers. This theory assumes that the interfaces are optically smooth and parallel, and provides the spectral directional radiative properties. The program assumes that there is no variation in properties over the azimuthal angel. Range allows the user to select a range of angles of incidence over which the spectral properties will be integrated. For example, choosing 0 to 90 will yield integration over the whole hemisphere (spectral hemispherical properties). Integrating over the whole hemisphere will increase the calculation time by approximately a factor of 25, relative to a single angle calculation. Calculation time decreases with decreasing size

of the range. Min/Max dictates the spectral range over which the properties are calculated. The limits of wavelength must be between 0.4 and 20 μm. Increment dictates the increment that the calculation will be done for. The minimum increment in wavelength is 0.001 μm. The smaller the increment, the more calculated are the data points, and so the longer the calculation will take.

It is possible to enter up to 100 layers. Light is incident, or emitted, from layer one. The layer material is already predefined. It is possible to choose between silicon, silicon dioxide, titanium silicide, silicon nitride, Gold, GaAs and SiO_2. Additional information such as temperature in degree C and layer thickness are necessary. For silicon, it is possible to enter the n and p dopant concentrations. In this version of Multi-Rad, silicon is the only material which has temperature dependent optical constants. Therefore, the temperature of the other materials has no effect on the result. The limits on temperature are between 30 and 1400 °C (melting point of Si). The output will be displayed in tabular form in the output box. The calculated results can be saved, exported and plotted. To calculate the total amount of energy that will be reflected, transmitted, emitted or absorbed in a certain spectral range, the spectral properties must be integrated with respect to wavelength for a certain black body distribution of energy. The emittance can also be interpreted as the absorptance of the wafer, depending on the spectral range and black body temperature chosen (i.e., the spectral emittance equals the spectral absorptance).

Directional analysis permits calculation of the optical properties at a particular wavelength as they vary with angle of incidence. The output will be a polar plot of the directional properties of stack at a particular wavelength. The program assumes that there

is no variation in optical properties over the azimuthal angle. It is possible to perform calculations over a single angle of incidence or a range of angles. The calculation is performed at a single detector wavelength. The program assumes a top-hat like profile for the detector response over bandwidth, reflecting the fact that all detectors have a finite bandwidth. For example, the emittance for a wavelength λ and bandwidth $\Delta\lambda$ is calculated by:

$$\varepsilon = \frac{1}{\Delta\lambda} \int_{\lambda-\frac{\Delta\lambda}{2}}^{\lambda+\frac{\Delta\lambda}{2}} \varepsilon_\lambda(\lambda)d\lambda \qquad (2.37)$$

Entering the stack is exactly as it is in the spectral analysis, described above.

The pyrometer option allows the user to calculate the radiative properties of a multilayer stack at a particular pyrometer wavelength. It also allows the user to examine the effect of film thickness variation on the radiative properties, and gives an estimate of the temperature measurement error that would be incurred by these variations. The angle of incidence works the same way as it does in the spectral analysis.

Pyrometer information necessary for calculations are the pyrometer wavelength and bandwidth. The pyrometer wavelength is the wavelength at which the pyrometer operates. The program assumes a top-hat like profile to the pyrometer response over the bandwidth. The nominal stack information is the same as in the spectral information. It is called "nominal" because it is meant to represent the target layer thicknesses.

Different options regarding the layer thickness variation are possible. No layer variation will allow calculation of the radiative properties for the nominal stack. One layer variation allows exploring the effect of varying the thickness of one of the layers in the stack on the radiative properties and temperature measurement error. It is possible to

enter the number of the layer whose thickness is varying. The minimum and maximum thickness of the layer and the thickness increment need to be entered. In order to calculate the temperature error, the nominal wafer temperature is also necessary. The calculation time is inversely proportional to the thickness increment. Two layer variations allow the user to vary the thickness of two layers in the stack. Now the calculation time will scale inversely proportional to the square of the increment, as calculating a 2D matrix. Again, the nominal wafer temperature needs to be entered. In the output display box, the results are displayed as a 2D rectangular matrix, with the thickness of the first layer along the first column and that of the second along the first row.

2.3.3 Adding Materials

It is also possible to add user materials. This option allows the user to customize the Materials List by adding new materials to the list. The user will be prompted to enter the name of the material as it is to appear in the materials list, and the names of two data files. These data files must be created off-line using a text editor. The first line of the first data file should be an integer indicating the number of data points to follow. All lines after that should contain two numbers: the wavelength and the refractive index. The second data file should have the same format as the first, except it should contain the data on the extinction coefficient. Multi-Rad does a simple linear interpolation between entered data points, so the user should make sure that there are enough points entered to capture features in the data. Calculations should not be done outside of the spectral range for which the refractive index and extinction coefficient data is entered.

2.4   Derivation of the Mathematical Model

The temperature distribution of a patterned wafer at the peak temperature of a RTP cycle is modeled by considering radiative and conductive heat transfer. The wafer is modeled as a two-dimensional system, where the thickness of the wafer t_w is small compared to the diameter. Temperature therefore can be taken to be uniform across the thickness of the wafer. The emission and absorption of radiation are treated as internal heat sources or heat sinks. Additional mechanisms which are excluded from the model include:

- Convection,

- Thermal contacts with the wafer,

- Heat radiation from the environment,

- Edge effects, i.e., the wafer is an infinite plane.

The radiation loss term given by Stefan-Boltzmann's T^4-law usually dominates over other loss mechanisms. However, the absorbed intensity is a quantity which is not directly measurable. This is modeled by relating the heat output intensity of the considered RTP system to the intensity absorbed by the wafer. This relation depends on the patterned layer structure on the wafer and the spectrum of the incident light which in many cases are not known in detail.

To validate the model, wafers with a square pattern were used in the experiment. A section of such a patterned wafer is shown in Figure 2.12. The derivation of the mathematical model is based upon this specific pattern structure.
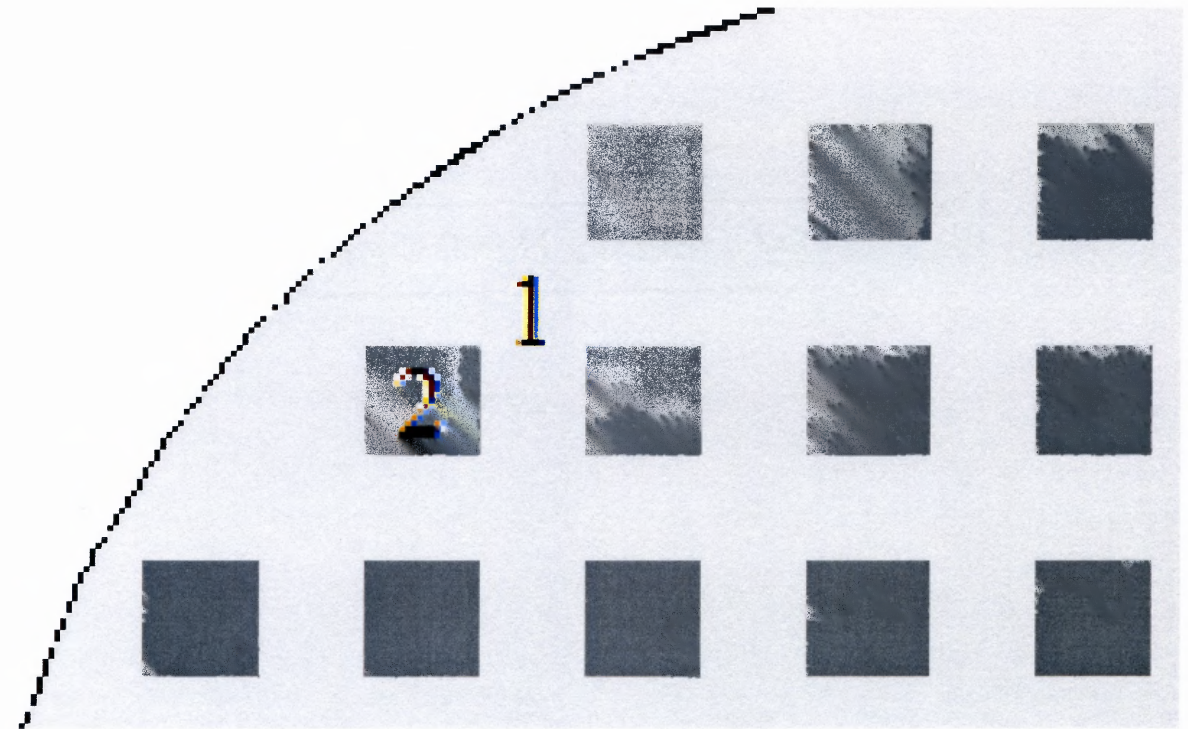
Figure 2.12 Schematic section of a square patterned wafer.

The pattern can be generally divided into two areas, 1 and 2. Area 1 and area 2 have different layers on top of the silicon wafer. These two areas have different emissivities and absorption coefficients. The index i=1, 2 refer to areas 1 and 2, respectively. The emissivity and absorption coefficient for area 1 is therefore denoted as ε_1 and α_1, respectively. For area 2, the optical coefficients are denoted as ε_2 and α_2. These optical coefficients are obtained by integration over incident angle and wavelength. Using the Stefan-Boltzmann law of radiation and the fact that the emitted and absorbed radiation intensities are equal in steady state, a heat balance equation can be established:

$$\sigma\alpha_2 T_F^{\ 4} + \sigma\alpha_3 T_B^{\ 4} = \sigma\varepsilon_2 T_2^{\ 4} + \sigma\varepsilon_3 T_2^{\ 4} \tag{2.38}$$

This equation is only for the area 2. A similar equation can be derived for area 1:

$$\sigma\alpha_1 T_F^{\ 4} + \sigma\alpha_3 T_B^{\ 4} = \sigma\varepsilon_1 T_1^4 + \sigma\varepsilon_3 T_1^4 \tag{2.39}$$

In these equations, T_1 and T_2 are the temperature of the respective areas. T_F is the temperature of the heat source impinging onto the wafer from the front and T_B is from the backside. Since a wafer has two sides, a third emissivity ε_3 and absorption coefficient α_3 is incorporated into the equation. These are the optical properties of the wafer backside. For a furnace process, T_F^4 is denoted as T_{FF}^4, and for a lamp process, T_F^4 is denoted as cT_{FL}^4, where c is a form factor that depends on the geometry of the lamp system. Both equations can be solved for the temperature of the areas (T_1 and T_2).

$$T_2^4 = \frac{\sigma\alpha_2 T_F^4 + \sigma\alpha_3 T_B^4}{\sigma\varepsilon_2 + \sigma\varepsilon_3}. \tag{2.40}$$

In this equation, the Stefan-Boltzmann constant σ can be canceled out.

$$T_2^4 = \frac{\alpha_2 T_F^4 + \alpha_3 T_B^4}{\varepsilon_2 + \varepsilon_3}. \tag{2.41}$$

Similarly for area 1:

$$\alpha_1 T_F^4 + \alpha_3 T_B^4 = \varepsilon_1 T_1^4 + \varepsilon_3 T_1^4, \tag{2.42}$$

$$T_1^4 = \frac{\alpha_1 T_F^4 + \alpha_3 T_B^4}{\varepsilon_1 + \varepsilon_3}. \tag{2.43}$$

Since T_1 and T_2 are unknown parameters, it is now possible to relate the temperature of both areas by dividing the equations for the temperature of areas 1 and 2:

$$\frac{T_1^4}{T_2^4} = \left(\frac{\alpha_1 T_F^4 + \alpha_3 T_B^4}{\alpha_2 T_F^4 + \alpha_3 T_B^4}\right)\left(\frac{\varepsilon_2 + \varepsilon_3}{\varepsilon_1 + \varepsilon_3}\right) \tag{2.44}$$

The important quantities for the radiation flux into an area i (i = 1, 2) are the radiation distributions and the effective emissivity and effective absorptivity of the surface. The effective emissivity and absorptivity take into account the specific optical

properties of the reflective chamber with all components inside. They depend on the material properties and temperature and are defined as spectral averages.

Lamp system

Wafer front side
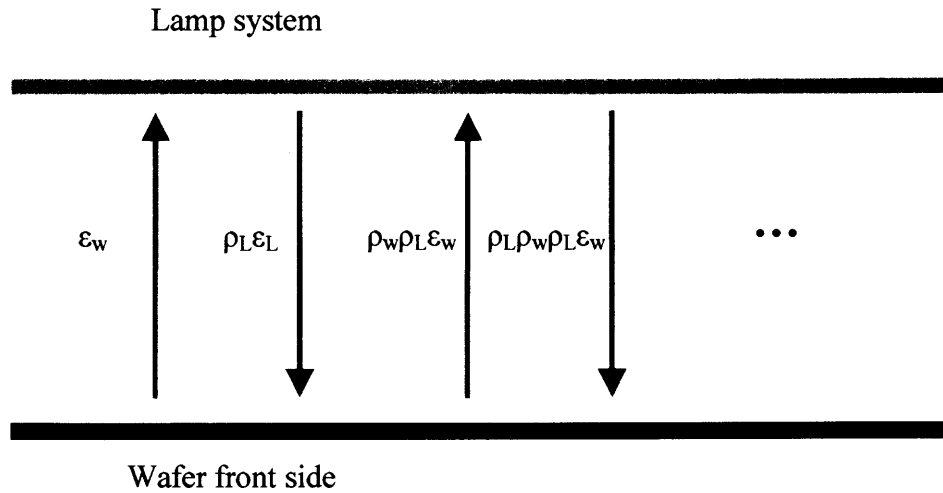
Figure 2.13 Reflection and back reflection within an RTP chamber.

These effective values are calculated by summing a series of multiple reflections, as shown in Figure 2.13. The series converges and can be described by an algebraic equation:

$$\varepsilon_{eff} = \frac{\varepsilon_W}{1 - \rho(1 - \varepsilon_W)}, \qquad (2.45)$$

and

$$\alpha_{eff} = \frac{\alpha_W}{1 - \rho(1 - \alpha_W)}, \qquad (2.46)$$

where, these values are then weighted by integrating the product of the emissivity as a function of wavelength, and the Planck distribution function:

$$\varepsilon_W = \frac{\int \varepsilon(\lambda) P(\lambda, T_w) d\lambda}{\int P(\lambda, T_w) d\lambda}$$

$$= \frac{\int \varepsilon(\lambda) \frac{2\pi h c_0^2}{\lambda^5} \frac{A}{e^{hc_0/(k\lambda T_w)} - 1} d\lambda}{\int \frac{2\pi h c_0^2}{\lambda^5} \frac{A}{e^{hc_0/(k\lambda T_w)} - 1} d\lambda}$$

(2.47)

For the sake of normalization, the Planck function also appears in the denominator. The Planck distribution is the black body radiation distribution at a certain temperature. The emissivity is calculated by using the Multi-Rad program. Multi-Rad uses a semi-empirical model for calculating the emissivity. The spectral analysis is performed over a wavelength range from 0.4 μm to 20 μm. It is averaged over incident angles from 0° to 90°. The increment in the calculation is $\Delta\lambda = 0.1$ μm.

The same approach is used for weighting the absorption coefficient:

$$\alpha_W = \frac{\int \varepsilon(\lambda) P(\lambda, T_F) d\lambda}{\int P(\lambda, T_F) d\lambda}$$

$$= \frac{\int \varepsilon(\lambda) \frac{2\pi h c_0^2}{\lambda^5} \frac{A}{e^{hc_0/(k\lambda T_F)} - 1} d\lambda}{\int \frac{2\pi h c_0^2}{\lambda^5} \frac{A}{e^{hc_0/(k\lambda T_F)} - 1} d\lambda}$$

(2.48)

The only difference between ε_w and α_w is the value of the temperature. For the emissivity, the temperature of the wafer is used, whereas for the absorption coefficient, the temperature of the heater, T_F, is used. Depending on the way of heating, the temperature for the absorption coefficient may differ for front side and backside. In the effective emissivity, no horizontal temperature gradient is assumed, i.e., front side and backside are assumed to be equal in temperature.

The one dimensional model used in the literature [17] includes the thermal conductivity. The model can be derived by using the heat balance equation:

$$\lambda(T)t_w \frac{\partial^2 T(x,t)}{\partial x^2} + q_{abs}(x,T) - 2\varepsilon(x,T)\sigma T(x,t)^4 = \rho C t_w \frac{\partial T(x,t)}{\partial t} \qquad (2.49)$$

Under steady-state, the time dependent term vanishes and Equation 2.49 becomes:

$$\lambda(T)t_w \frac{d^2 T(x)}{dx^2} + q_{abs}(x,T) - 2\varepsilon(x,T)\sigma T(x)^4 = 0 \qquad (2.50)$$

where, $\lambda(T)$ is the thermal conductivity, t_w is the thickness of the wafer and $q_{abs}(x,T)$ is the absorbed energy density. Using the relation for $T(x) = T_0 + \Delta T(x)$, Equation 2.50 becomes:

$$\lambda(T)t_w \frac{d^2 \Delta T(x)}{dx^2} + q_{abs}(x,T) - 2\varepsilon(x,T)\sigma T_0^4 - 8T_0^3 \varepsilon(x,T)\sigma \Delta T(x) = 0 \qquad (2.51)$$

Solving this differential equation leads to the lateral thermal diffusion length:

$$L_d = \sqrt{\frac{\lambda t_W}{8\varepsilon\sigma T^3}} \qquad (2.52)$$

This model can be expanded in two dimensions. Then, all space dependent variables are a function of x and y. The pattern shown in Figure 2.12 is represented by two-dimensional periodicity of spacing L. The square pattern can thus be defined by a two-dimensional Fourier-series for a symmetrical square wave:

$$
\begin{aligned}
P(x,y) = \frac{1}{4} + \sum_{n=1,3,...} \frac{1}{\pi n}(-1)^{\frac{n-1}{2}} \cos(k_n x) + \sum_{n=1,3,...} \frac{1}{\pi n}(-1)^{\frac{n-1}{2}} \cos(k_n y) \\
+ \frac{1}{4}\sum_{n=1,3,...} \frac{4}{\pi n}(-1)^{\frac{n-1}{2}} \cos(k_n x) \sum_{n=1,3,...} \frac{4}{\pi n}(-1)^{\frac{n-1}{2}} \cos(k_n y)
\end{aligned} \qquad (2.53)
$$

where, $k_n = 2\pi n / L$. The coordinates are x and y aligned parallel to the square edges and the origin is in the square center. This equation is used to express the emissivity and

absorptivity in terms of x and y. An unknown temperature distribution can be represented by a two-dimensional Fourier series with coefficients, t_n.

$$\Delta T(x,y) = \frac{1}{4}\left(1 + \sum_{n=1,3,\ldots} t_n(-1)^{\frac{n-1}{2}}\cos(k_n x)\right)\left(1 + \sum_{n=1,3,\ldots} t_n(-1)^{\frac{n-1}{2}}\cos(k_n y)\right). \quad (2.54)$$

Equation 2.53 and 2.54 are then substituted into an equation of the form:

$$c_1\nabla^2\Delta T(x,y) - c_{10}P(x,y)\Delta T(x,y) + c^{**}P(x,y) - c_8\Delta T(x,y) + c^* \quad (2.55)$$

and Equation 2.55 is then solved for the unknown Fourier coefficients t_n. The exact solution is given in Appendix A. The solution is simplified by considering only high symmetry points in the pattern and relating the temperatures at these points to the temperature at the reference point, i.e., the origin.
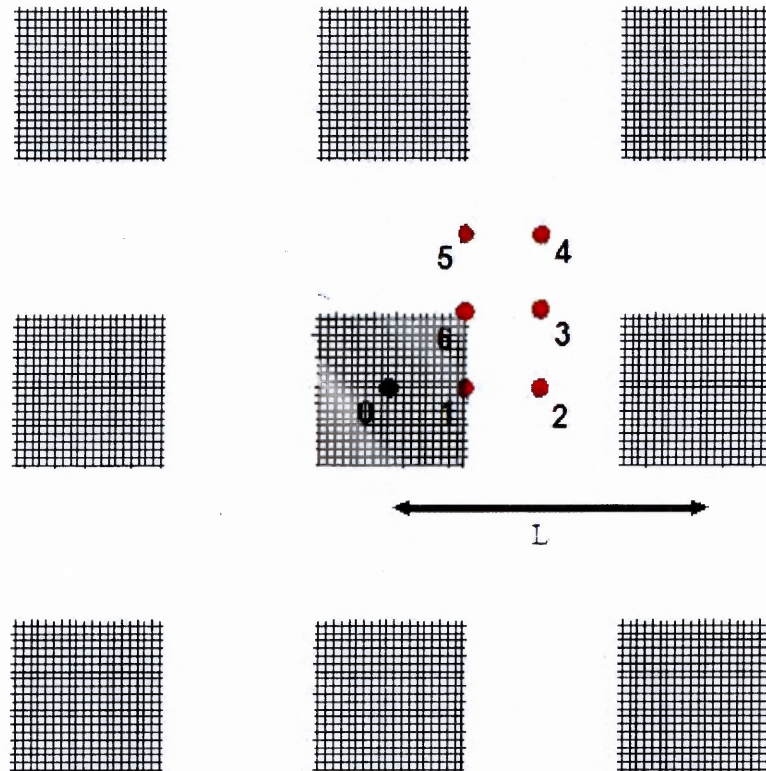
Figure 2.14 Square pattern with periodicity L. High symmetry points are denoted as 0, 1, ..., 6.

The reference point in Figure 2.14 is in the center of the square. The temperatures at the symmetry points, determined in Equation 2.54, can be expressed in terms of cosine functions that correspond to -1, 0, or 1. Table 2.3 gives the cosine values and expressions for $\Delta T(x,y)$ at the points in Figure 2.14.

Table 2.3 Values of Cosines and ΔT at High Symmetry Points

Point	cos(x)	cos(y)	$\Delta T(x,y)$
0	1	1	$\frac{1}{4}\left(1+\sum_{n=1,3,\ldots} t_n(-1)^{\frac{n-1}{2}}\right)\left(1+\sum_{n=1,3,\ldots} t_n(-1)^{\frac{n-1}{2}}\right)$
1	0	1	$\frac{1}{4}\left(1+\sum_{n=1,3,\ldots} t_n(-1)^{\frac{n-1}{2}}\right)$
2	-1	-1	$\frac{1}{4}\left(1-\sum_{n=1,3,\ldots} t_n(-1)^{\frac{n-1}{2}}\right)\left(1+\sum_{n=1,3,\ldots} t_n(-1)^{\frac{n-1}{2}}\right)$
3	-1	0	$\frac{1}{4}\left(1-\sum_{n=1,3,\ldots} t_n(-1)^{\frac{n-1}{2}}\right)$
4	-1	-1	$\frac{1}{4}\left(1-\sum_{n=1,3,\ldots} t_n(-1)^{\frac{n-1}{2}}\right)\left(1-\sum_{n=1,3,\ldots} t_n(-1)^{\frac{n-1}{2}}\right)$
5	0	-1	$\frac{1}{4}\left(1-\sum_{n=1,3,\ldots} t_n(-1)^{\frac{n-1}{2}}\right)$
6	0	0	0

Denoting $S = \sum_{n=1,3,\ldots} t_n(-1)^{\frac{n-1}{2}}$, leads to the following equations:

$$\Delta T(1) = \frac{1}{4}(1+S)(1+S) = \frac{1}{4} + \frac{1}{2}S + \frac{1}{4}S^2, \qquad (2.56)$$

$$\Delta T(2) = \frac{1}{4}(1+S), \qquad (2.57)$$

$$\Delta T(3) = \frac{1}{4}(1-S)(1+S) = \frac{1}{4} - \frac{1}{4}S^2, \qquad (2.58)$$

$$\Delta T(4) = \frac{1}{4}(1-S), \qquad (2.59)$$

$$\Delta T(5) = \frac{1}{4}(1-S)(1-S) = \frac{1}{4} - \frac{1}{2}S + S^2. \qquad (2.60)$$

In the limit for L $\to \infty$, S $\to$ 1. This limit implies that the pattern is decomposed

in two different wafers with infinite extension. Wafer 1 is like the field and wafer 2 is like

the square. By determining S, experimentally, one can obtain a result for $\dfrac{T_1^4}{T_2^4}$ in Equation

2.44.

CHAPTER 3

SPECIFIC PROCESS MODES AND EXPERIMENTS

The heating process in RTP follows a certain recipe for the temperature versus time profile. Process modes differ according to the way in which the intensity is controlled. One method is just to supply a certain power level to the lamps without controlling the temperature directly. This is known as the open-loop intensity control (OLIC). If the temperature is controlled by an error feedback, it is referred to as closed loop temperature control heating. The objective of closed loop temperature control (CLTC) is a more accurate temperature control approach, in contrast to the OLIC.

3.1   Open-Loop Intensity Control (OLIC)

In open loop intensity control, the wafer is placed into the chamber and the lamps are supplied with constant power. The power control of OLIC operates under the assumption that if the same power is delivered to the lamps, then the same intensity will be emitted. Thus, if the wafer and process chamber conditions do not vary, then the absorption of the intensity by the wafer will be constant. The issues with power control are chamber window and wall hazing altering the absorption and reflection properties of the wafer environment, lamp aging, wafer variations, and line voltage regulation.

The OLIC was tested on wafers with various backside films and an RTO process on the front side. Temperature distributions are inferred in this process by the oxide film thickness. With a constant recipe, it is assumed that there is a relation between power input, temperature, and oxide thickness. Beforehand calculations were done to find out

52

the power requirement for these conditions. The tacit assumption is that the absorption, emissivity and reflectivity are the same for a layered wafer as it is for the bare silicon wafer used for steady-state temperature calibration. The chamber was pre-heated to try to give all wafers the same initial condition, but the first wafer was always a dummy wafer. Temperatures during RTO processing were measured by pyrometers and thermocouples.

Film thicknesses on the backside of the wafers were determined from separate monitor wafers. The wafers under test were p-bulk from various slots, except for one which was an epitaxial wafer. Bare wafers from several batches were included for reference points. Table 3.1 gives an overview of the wafers used in the experiments.

Table 3.1 Wafers Backside Films Used in the Experiment

Slot	Wafer ID	Backside Films [Å]			
1	B1-10	Bare Si-wafer			
2	E1-2	200 Oxide	2400 Nitride	1550 Oxide	290 Poly
3	E2-4	200 Oxide	2400 Nitride	1550 Oxide	850 Poly
4	E3-18	200 Oxide	2400 Nitride	1550 Oxide	1660 Poly
5	E4-20	200 Oxide	2400 Nitride	1550 Oxide	
6	H1-13	1000 Poly /100 Oxide	930 Nitride	1030 Oxide	
7	B2J-7	Bare Si-wafer			
8	J1-24	5000 Oxide	600 Poly		
9	J2-1	2000 Oxide	3500 Poly		
10	J2-7	2000 Oxide	3500 Poly		
11	J2-13	2000 Oxide	3500 Poly		
12	J5-19	5500 Oxide	5000 Poly		
13	B2K-1	Bare Si-wafer			
14	K1-16	3900/4700 Oxide			
15	L1-10	2560 Oxide	580 Poly	480 Nitride	
16	L2-22	5000 Oxide	2000 Poly	480 Nitride	
17	O1E	p+ Epi	200/225 Oxide	600 Poly	500/2400 Nitride
18	B1-11	Bare Si-wafer			
19	B2K-2	Bare Si-wafer			

The polysilicon layers were undoped. They were annealed in a furnace after CVD deposition. The oxide films include an underlying furnace oxide and CVD-PE-TEOS deposited films that are RTA densified. Some nitride films were similarly deposited and annealed.

Initially, the wafers were cleaned by an HF-RCA clean, which leaves 5 to 7 Å of chemical oxide on the wafers. RCA clean with HF dip is a standard pre-furnace cleaning step to avoid diffusion of contaminants into the wafer. The hydrofluoric acid (HF) preferentially etches the silicon dioxide, but not the silicon. It also removes organics, particles and some metals. The wafers are first immersed in a hot mixture of ammonium hydroxide (NH_4OH), hydrogen peroxide (H_2O_2) and deionized (DI) water in a ratio of 1:1:5. This removes traces of organic residues and when done on exposed silicon surfaces, traps ionic contaminants such as sodium and potassium in a thin oxide.

The wafers are then rinsed in a quick dump rinser (QDR) which provides a fast method of rinsing, allowing wafers to be moved quickly from one step to the next. Next, the thin layer of silicon dioxide (SiO_2) is removed by dipping in dilute hydrofluoric acid (HF). Another QDR cycle follows. Then the wafers are immersed in a mixture of hot hydrochloric acid (HCl), H_2O_2, and DI water. The ratio is again 1:1:5. This mixture is effective for removal of ionic contaminants, especially metals. The wafers are again rinsed in the QDR. A final HF and QDR step is optional. Then the wafers are spun dry and are ready for the lamp RTO process [18].

In the open loop intensity control recipe, the recipe time per wafer was 15.7 min. At the beginning of the process, the wafer was placed into the RTP chamber. It was placed in such a way that the layers were on the backside and bare silicon was on the

front side. The wafer was exposed to 20 % N_2 for 600 s. Then the N_2 concentration was decreased to 10 %, and the O_2 concentration was increased from 0 % to 8 % for 10 s. In the third step, with duration of 20 s, the N_2 concentration was reduced to 0 and the O_2 concentration was decreased to 5 %. In the last step, before the heating step was implemented, the wafer was exposed to an O_2 concentration of 3 % for 30 s. The lamps were then turned on to an intensity of 42.5 % with a rate of 10 %/s. After reaching an intensity of 42.5 %, the lamp intensity was kept constant for 60 s. In this 60 s, the O_2 concentration was kept at 3 %. The supplied intensity of 42.5 % for 60 s heated the wafer to about 1090 °C. The lamps were then switched off. After 10 s, the O_2 supply was also switched off and the N_2 concentration was increased from 0 to 5 %. In the last step, the N_2 concentration was further raised to 20 % for duration of 220 s.

A ripple pyrometer was used for temperature measurements. The ripple pyrometer compensates for unknown variable emissivity of wafers and removes interference from reflected radiation from the heating lamp. In other words, it separates the wafer emittance radiation from reflected lamp radiation and simultaneously finds the wafer emissivity in situ. Power to the heating lamps is modulated with oscillatory functions of time. Therefore, two separate input optics, one for wafer radiation and the other as a reference for the lamp radiation is used. The electrical signals are separated into a slowly varying quasi-steady and a rapidly varying ripple component. The slowly varying components represent the radiation from the wafer.

The ripple signals are digitally processed to find the component of the lamp radiation that is reflected by the wafer under the assumption of negligible wafer temperature oscillation at the ripple frequencies. The ripple signal analysis yields a

measure of the wafer reflectivity that is used to compute an effective wafer emissivity. It also allows subtracting lamp interference to yield a more slowly varying signal for the thermal radiance of the wafer. The analysis interval was from 45 s to 55 s. Table 3.2 gives the temperatures measured by direct thermocouple (DTC), the emissivity uncompensated pyrometer (PYRO) and the ripple pyrometer (RPL), i.e., the temperature during the process. All values of temperature are averages over the time interval from 45 s to 55 s measured from the time the lamps are turned on.

Table 3.2 Temperatures Measured with Thermocouple, Pyrometer and Ripple Pyrometer

Wafer ID	DTC	PYRO	RPL
B1-10	1091.2	1100.9	1087.2
E1-2	1088.9	1156.3	1085.5
E2-4	1084.6	1201.5	1051.1
E3-18	1087.3	1165.2	1061.3
E4-20	1089.3	1148.4	1087.0
H1-13	1089.8	1110.7	1095.9
B2J-7	1088.1	1086.5	1085.4
J1-24	1085.3	1201.0	1043.2
J2-1	1085.6	1164.7	1024.7
J2-7	1085.3	1165.4	1024.6
J2-13	1085.1	1165.0	1024.6
J5-19	1091.6	985.4	1094.2
B2K-1	1089.7	1087.5	1087.2
K1-16	1086.1	1125.7	1091.9
L1-10	1091.9	988.6	1079.5
L2-22	1093.7	857.5	1097.3
O1E	1088.2	1172.5	1076.8
B1-11	1087.3	1091.4	1083.3
B2K-2	1088.3	1085.2	1085.3

After the process was complete, the oxide thickness was measured with the Thermawave at 52 points. An area corresponding to 5 mm on the edges of the wafer was excluded from the measurements. Table 3.3 summarizes the measured oxide thicknesses.

Table 3.3 Thermawave Measurements of Oxide Thicknesses

Wafer ID	Average	Sigma	Range
B1-10	69.54	1.11	7.37
E1-2	69.77	1.03	7.23
E2-4	68.23	1.11	8.13
E3-18	76.13	0.95	5.76
E4-20	67.47	0.74	6.41
H1-13	75.87	1.07	6.37
B2J-7	70.89	0.65	4.40
J1-24	71.72	1.39	8.30
J2-1	44.51	0.90	11.40
J2-7	44.56	0.91	10.91
J2-13	44.88	0.87	10.38
J5-19	51.10	1.48	12.02
B2K-1	70.44	0.93	5.56
K1-16	77.26	0.96	4.70
L1-10	71.08	0.81	5.23
L2-22	54.63	0.64	5.36
O1E	53.71	0.90	8.68
B1-11	70.62	0.76	4.10
B2K-2	74.67	1.48	7.75

Comparison of the temperature measured by the ripple pyrometer in Table 3.2 with the oxide thicknesses in Table 3.3 shows correlations where the oxide thickness tends to increase with the temperature. For example, wafers in the J2 series were heated to a temperature near 1025 °C, which is at the low end of the temperature range, and corresponds to an oxide thickness of 45 Å, which is at the low end of the oxide thickness range. Other wafers were heated to higher temperatures and the oxide thicknesses were greater but the correlation between the two is not a perfect one. These results show that OLIC does not yield a wafer independent process for RTO. This is a strong motivating factor for selecting closed loop temperature control, which is treated in the next section.

3.2 Closed Loop Temperature Control (CLTC)

If coatings on the wafer are present, then the coated regions will experience different temperature-time cycles during processing than the uncoated regions, leading to a significant impact on process uniformity. RTP systems are usually operated in the temperature mode by performing a closed loop temperature control by a calibrated optical pyrometer or thermocouple. This can be achieved with a pyrometer that measures the wafer temperature and provides feedback to the control system, such as shown in Figure 3.1 [8]. The challenge is to perform highly accurate pyrometric measurements on a wafer of unknown spectral emissivity in surroundings in which a significant amount of stray radiation may be emitted by the heat source.
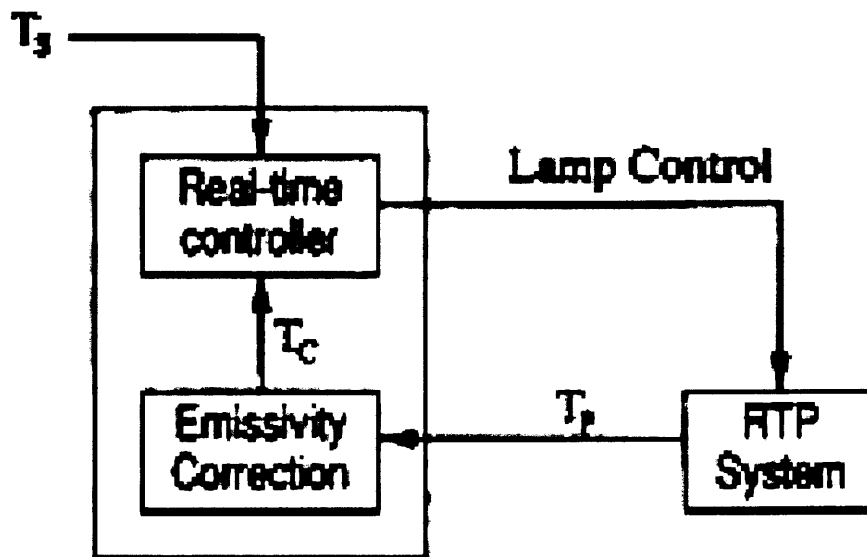
Figure 3.1 RTP control system with emissivity correction [8].

Although the incident intensity differs from the absorbed intensity, only the absorbed intensity influences the closed loop temperature control to match the actual temperature-time profile to the desire one. Therefore, the absorption characteristics have to be known. For the purpose of the calculations, an ideally controlled temperature is

assumed. The temperature at the measured spot is assumed to be given at any time by the pre-set temperature time cycle. A signal from an appropriate thermal sensor, thermocouple or pyrometer controls the feedback loop and determines the power to the lamps [8].

In this thesis, all RTP systems that were used to test the model were operated with model based temperature control. Model based temperature control needs to be tuned through temperature data logs of the actual temperature in the chamber during an entire process cycle. Figure 3.2 [8] shows a model based temperature control system with a thermocouple to measure the wafer temperature. Model based temperature control is based on systematic use of a mathematical model of the process in determining control algorithms for the process.
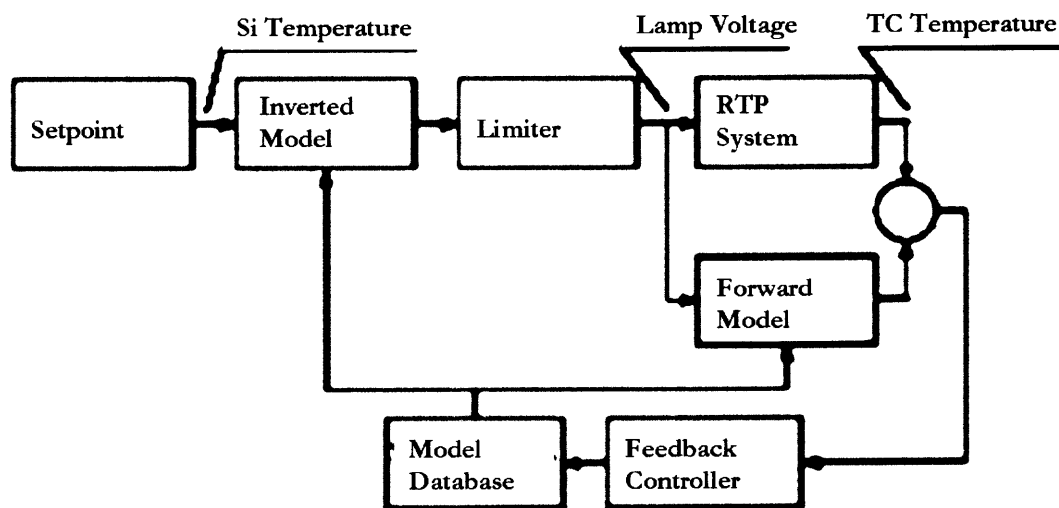
Figure 3.2 Schematic of model based feedback loop with TC control [8].

Another possibility is to use a proportional integral differential (PID) control. Precision wafer temperature estimation and control is more critical in RTP due to the lag of the thermocouple relative to wafer temperature under fast ramping conditions. A

proportional integral differential (PID) controller can overshoot the desired temperature and needs more time to tune due to the lag time. Model based temperature has the ability to predict the discrepancy between these two parameters and allow to accurately control wafer temperature during dynamic conditions.

The control design relies on the experimental data obtained from the reactor to be controlled. The system closed-loop behavior is dependent on both the hardware design and the controller design. The advantage of the closed-loop simulation is that it allows for quantifying the response to a potential disturbance. Decreasing the feedback gain can lead to sluggish response resulting in unacceptable temperature non-uniformity and tracking error. Increasing the gain can create power demands that exceed the range of actuation resulting in power saturation and loss of control.

To evaluate lateral temperature non-uniformities during RTP, two indirect measurement techniques were used in these studies:

- Annealing of a high dose, low energy As-implantation (wafer maps of sheet resistance)

- Rapid thermal oxidation

The sheet resistance of As-implanted Si upon RTA can be correlated with wafer temperature using a calibration curve. Hence, wafer maps of sheet resistance can be interpreted as lateral temperature measurements on the wafer. The sheet resistance depends on activated dopants and the activation process is temperature dependent. Hence, partial activation of ion implanted species is very suitable to measure and optimize the across wafer uniformity. The data were converted into effective temperatures using a linear model for dependence of mean post-RTA sheet resistance on temperature. A common disadvantage of both indirect methods is that they integrate all variations from

the defined processing recipe into a single parameter. Even if the final temperature distribution across the wafer is acceptable, there could be a part of the processing interval in which temperature non-uniformity is above the limit of acceptance.

The model uses four temperature states: lamp filament temperature, quartz temperature, pyrometer temperature and TC temperature. A set of four first order, non-linear differential equations describe the model. Feedback is achieved by updating the model, based on a comparison between actual (measured) system and modeled system response. The Model Based Control uses two steps to reach a tight match between the set point temperature and wafer temperature. In the first step, the 4 state model of the system is inverted to predict that level of power input or position that will drive the wafer temperature to reach the set point temperature. The inverted model transforms Si temperature into predicted lamp voltage or position. In most cases, the calculated voltage or position is limited between a maximum and minimum value. Due to this limitation, a perfect match is not always possible. This leads to a limit on the first and second order deviations of temperature. In the second step, the actual lamp voltage or position (after clipping) is used as input of the forward model to calculate a prediction of the indicated TC temperature. Any offset between the predicted TC temperature and the measured TC temperature is used to adjust the model. The forward model is used to calculate the TC temperature (not the Si temperature). In general, any parameter of the model (in the model data base) could be tuned in real time while the control is active. An optimization method can be used to tune the chamber efficiency, which is dependent mainly on wafer absorptivity, during temperature ramps and to tune the wafer emissivity during steady state [8].

3.3 Model Validation Experiments

The model described in Section 2.5 was tested by annealing wafers with square patterns. Temperature profile was inferred from the sheet resistance of an As-implanted wafer. The process steps were:

1) Clean wafers and grow pad oxide

2) Implant As^+ at a 20 kV and 10^{16} cm^{-2}

3) Deposit 110 nm SiO_2

4) Deposit 100 nm polycrystalline silicon

5) Pattern squares etched by removing polycrystalline silicon

6) RTA process

7) Strip off pattern films

8) Measure sheet resistance

The RTA process was a spike anneal with a temperature versus time profile of the type idealized and shown in Figure 3.3 [8] with constant ramping rates α_{up} and α_{down} and steady temperature T_{max} at the peak. The definition of spike assumes that this is achieved by heating as fast as possible to the desired temperature and immediately cooling as fast as possible with minimal dwell time at peak temperature. In practice, the actual temperature profile is shown for the furnace process in Figure 2.5 and for the lamp process in Figure 2.9. In modeling the spike anneal, the process temperature is taken to be T_{max}.
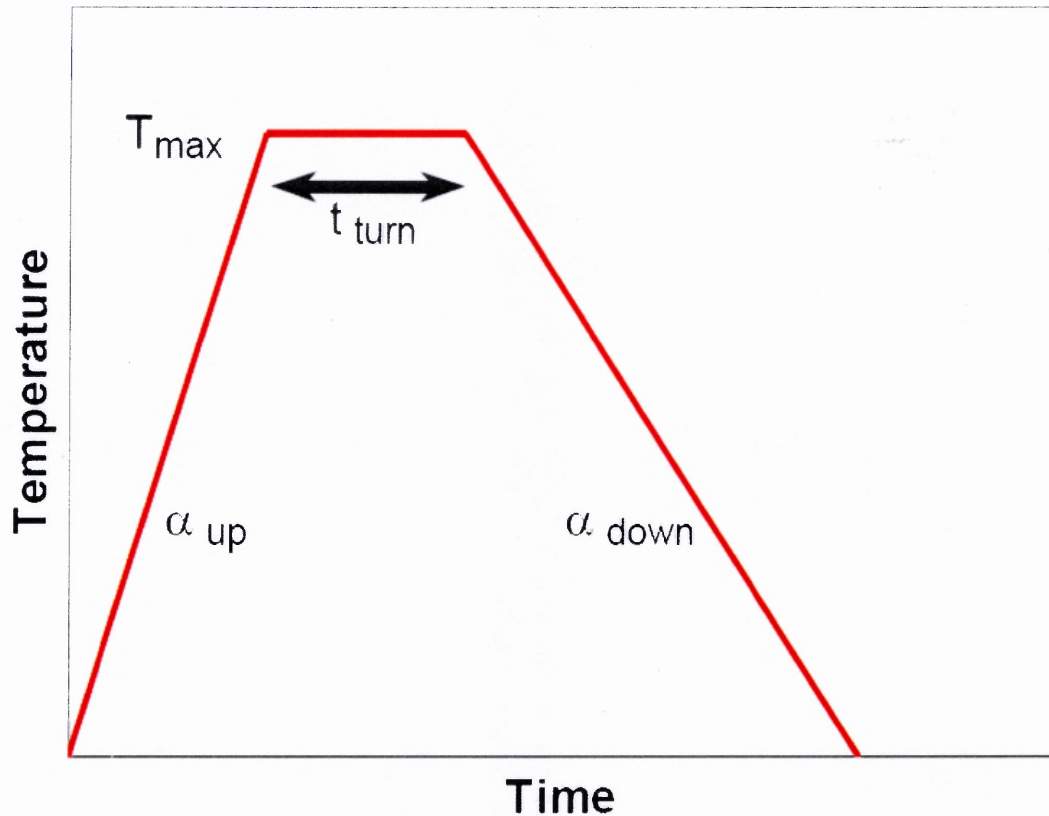
Figure 3.3 Idealized spike process [8].

In this work, the spike process was realized in furnace and lamp RTP systems with three different kinds of wafers. In the lamp RTP system, the power input is controlled. In the furnace system, the wafer position in the furnace is controlled. As discussed previously, in the furnace system, the power is kept constant, i.e., the furnace is heated steadily. A temperature gradient is realized within the furnace and the wafers are elevated in the furnace. The temperature in a furnace is a function of the position. The wafers under test were bulk wafers, epitaxial wafers and SOI wafers (SIMOX), as illustrated in Figure 3.4.
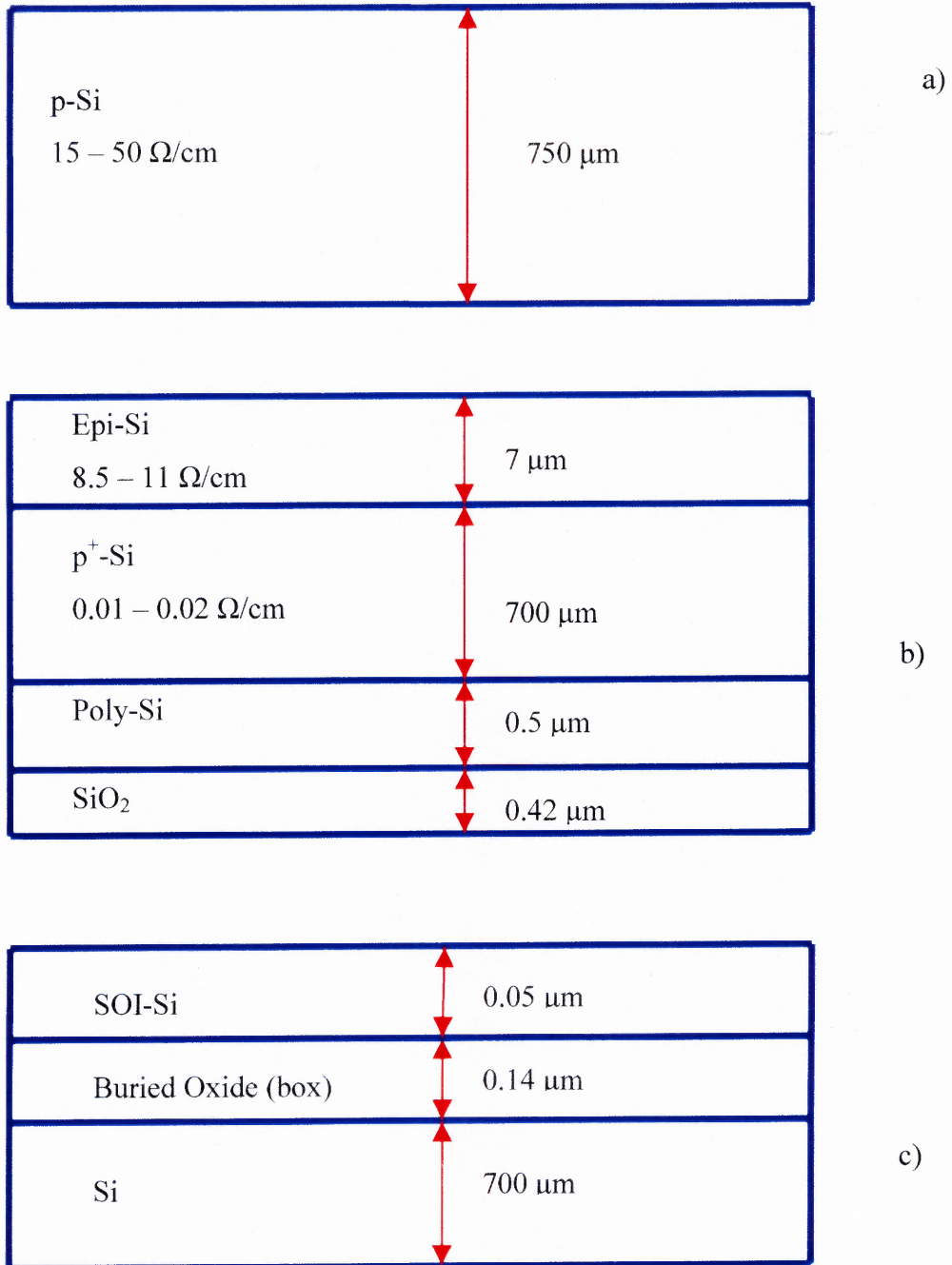
Figure 3.4 Cross sections of a) bulk, b) epitaxial, and c) SOI wafer.

Each of these wafers were coated with SiO_2 and polysilicon layer. For realizing the pattern, the polysilicon layer was etched away in a square pattern. The Figure 3.5 shows the schematics of the wafers after they were etched. Figure 3.6 is a full wafer view of the front side pattern, which is an array of 1 cm x 1 cm squares, spaced $L = 2$ cm apart.

Poly-Si
SiO$_2$

p-Si

a)

Poly-Si
SiO$_2$
Epi-Si

p$^+$-Si

Poly-Si
SiO$_2$

b)

Poly-Si
SiO$_2$
SOI-Si
Buried Oxide (box)

Si

c)
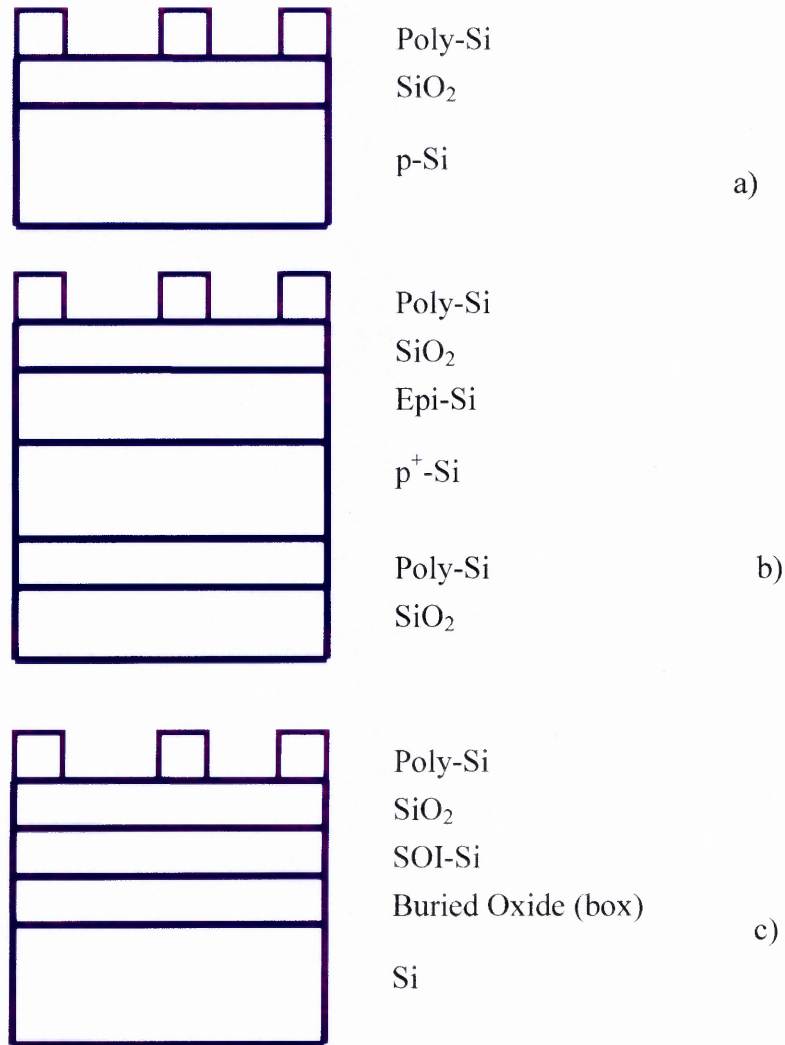
Figure 3.5 Wafers after the etch process.

The measured thicknesses of the layered structures are shown in Tables 3.4 and 3.5:

Table 3.4 Measured Specification of Layers on Bulk, Epitaxial and SOI Wafers

Thermawave		Film thicknesses [Å]				
		Poly	Oxide	Si	buried Oxide (box)	GOF
SOI	etched part	0	886	543	1449	0.92
SOI	etched part	0	887	543	1450	0.92
SOI	etched part	0	882	536	1444	0.92
Bulk	etched part	0	786			0.9879
Epi	etched part	0	825			0.9947
SOI	unetched part	1053	1122	501	1432	0.93
SOI	unetched part	1053	1112	510	1440	0.93
SOI	unetched part	1051	1136	508	1419	0.93
Bulk	unetched part	1056	1002			0.9083
Epi	unetched part	1114	1093			0.9143
Cross section of unpatterned SOI wafer				500	1100	
SOI wafer specs:				550	1450	
mean	etched part		853.2			
mean	unetched part	1065.4	1093			
standard deviation	etched part		45.7132366			
standard deviation	unetched part	27.22682501	53.22593353			

Table 3.5 Measured Specifications of Bulk, Epitaxial and SOI Wafers

Thermawave		Poly	Film thicknesses [A]			GOF
			Oxide	Doped-Si	buried Oxide (box)	
SOI (Pre-Anneal)	etched part	0	882.66	542.85	1451.22	0.9227
SOI (Pre-Anneal)	etched part	0	884.56	544.86	1452.56	0.9218
SOI (Pre-Anneal)	etched part	0	878.66	537.24	1445.26	0.9212
SOI (Pre-Anneal)	unetched part	1049.54	1158.99	485.02	1484.4	0.9311
SOI (Pre-Anneal)	unetched part	1050.98	1158.99	484.86	1495.11	0.9306
SOI (Pre-Anneal)	unetched part	1051.5	1150	479.59	1489.65	0.9303
Cross section of unpatterned SOI wafer				500	1100	
SOI wafer specs:				550	1450	
mean	etched part		881.96			
mean	unetched part	1050.673333	1155.993333			
standard deviation	etched part		3.011644069			
standard deviation	unetched part	1.015348873	5.19037892			

Thermawave			Resistance [Ohm-cm]	Wafer thicknesses [A]		Emissivity(backside)
Bulk		p-type	15-20	7000000	7500000	
Epi				7100000	7400000	0.706-0.712
Epi-layer		p-type	8.5-11	63000	77000	
Epi-substrate		p-type	0.01-0.02			
SOI						0.682

Figure 3.6 Square patterns on the wafers.

The wafers were placed in the chamber in a way such that the pattern was on the front side. In the case of the lamp system, only the front side was heated, whereas in the furnace, both sides were heated. Different measurement methods for wafer temperature were used. Multi-Rad was used to calculate the spectral emissivities of the wafer at T_{max} = 1050 °C corresponding to the RTA process. This quantity is multiplied by the Planck function. In Figures 3.7, 3.8 and 3.9, the emittance are plotted as function of wavelength for bulk, epitaxial and SOI wafers at room temperature, 600 °C and 1000 °C, respectively.
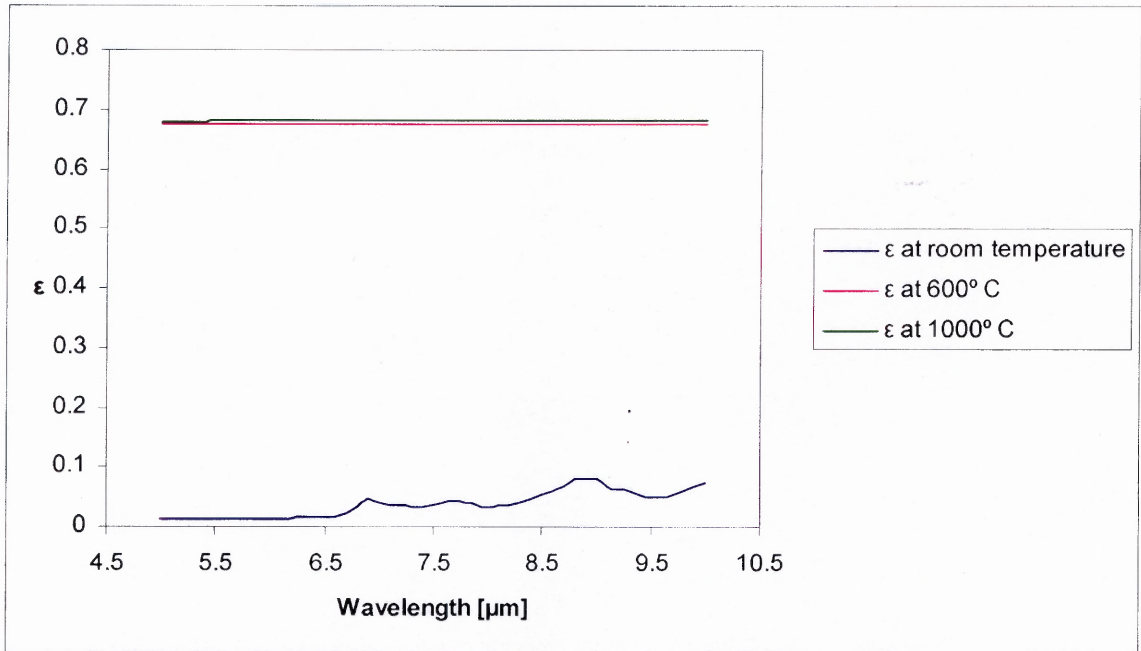
Figure 3.7 Calculated emittance versus wavelength of a bulk wafer at different temperatures.
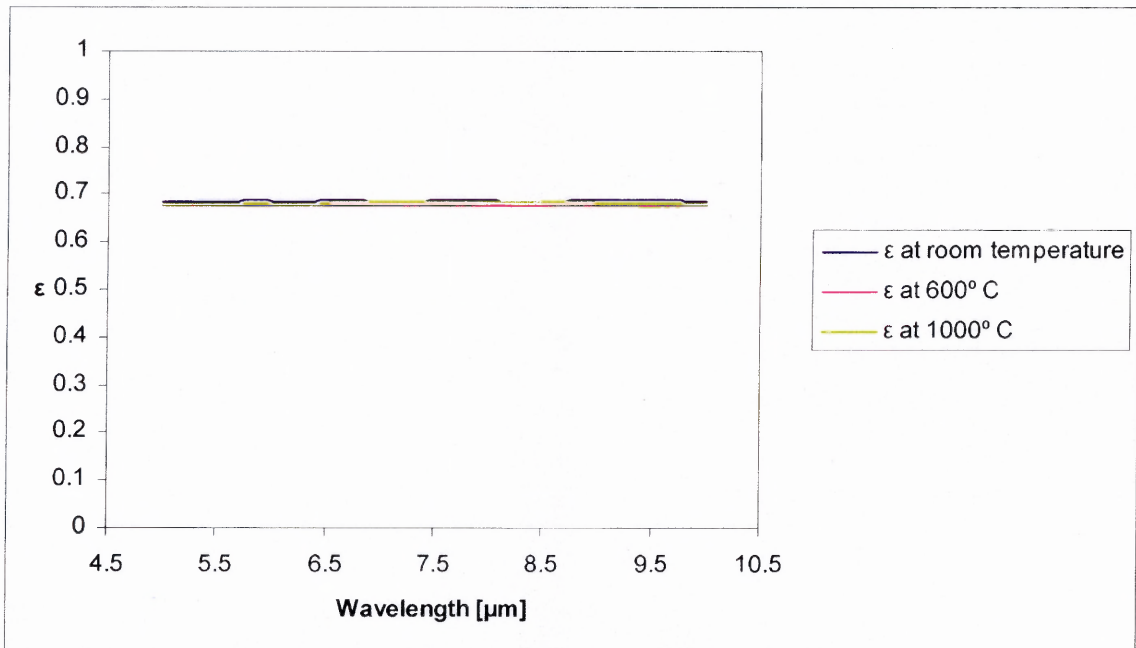
Figure 3.8 Calculated emittance versus wavelength of a epitaxial wafer at different temperatures.
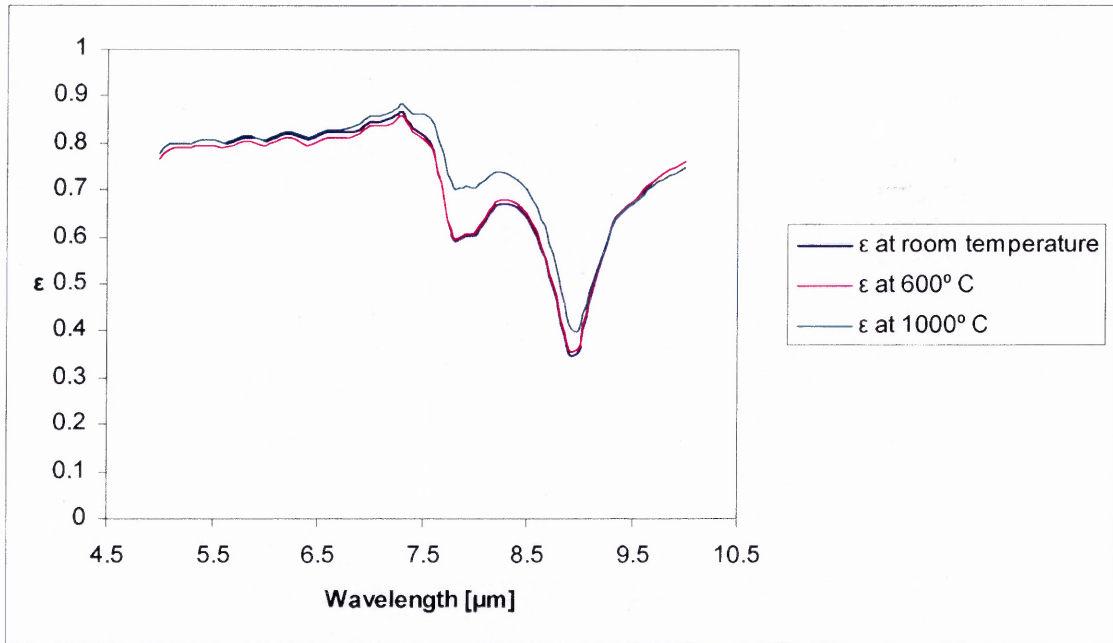
Figure 3.9 Calculated emittance versus wavelength of a SOI wafer at different temperatures.

After integrating and normalizing these curves, the emissivities and absorptivities shown in Tables 3.6 to 3.9, were calculated. For the emissivities, the temperature refers to the wafer temperature. For the absorptivities, the temperature refers to the heater temperatures.

Table 3.6 Calculated Emissivity at 1050 °C

T = 1323 K	Field Front side ε_1	Square Front side ε_2	Backside ε_3
Bulk p-Wafer	0.703	0.676	0.671
Epitaxial Wafer	0.703	0.678	0.779
SOI Wafer	0.654	0.777	0.671

Table 3.7 Calculated Absorptivity for Furnace Process (Front side) at 1250 °C

T = 1523 K	Field Front side a_{FT1}	Square Front side a_{FT2}
Bulk p-Wafer	0.672	0.676
Epitaxial Wafer	0.672	0.678
SOI Wafer	0.621	0.756

Table 3.8 Calculated Absorptivity for Furnace Process (Backside) at 850 °C

T = 1123 K	Backside α_{FB3}
Bulk p-Wafer	0.673
Epitaxial Wafer	0.767
SOI Wafer	0.673

Table 3.9 Calculated Absorptivity for Lamp System at 2377 °C

T = 2650 K	Field Front side α_{L1}	Square Front side α_{L2}	Backside α_{L3}
Bulk p-Wafer	0.548	0.678	0.654
Epitaxial Wafer	0.548	0.686	0.762
SOI Wafer	0.513	0.584	0.654

Calculations were performed at a wafer temperature of 1050 °C. The wavelength range was between 0.4 and 20 μm with an increment $\Delta\lambda = 0.1$ μm. The values calculated with Multi-Rad are all hemispherical emissivities. As can be seen from the Table 3.7, the backside emissivity of the bulk p-wafer and the SOI-wafer are equal. Both wafers do not have any layers on the backside, whereas the epitaxial wafer has a polysilicon/SiO_2-layer. At the front side, the bulk and epitaxial wafer have a similar emissivity. The SOI wafers differ in greater magnitude in emissivity, especially for the case in which the polysilicon is etched away. It can be inferred that the buried oxide influences the emissivity.

The values of emissivity for the furnace process were calculated as follows. In the furnace process, the heating of the wafer is from both sides. For the furnace, a temperature of $T_{FU} = T_W \pm 200$ °C is assumed, where T_W is the wafer temperature (1050 °C). Hence, the upper furnace temperature is $T_{FT} = 1250$ °C and the lower temperature $T_{FB} = 850$ °C. For the lamp system, temperature of $T_L = 2650$ °K ≈ 2377 °C was used.

In the furnace heating, a reflection coefficient for the upper part of the chamber of 0.05 and for the lower part of the chamber of 0.15 is defined. The results for the effective emissivity were obtained by utilizing Equations 2.44 and 2.45 and are shown in Table 3.10.

Table 3.10 Calculated Effective Emissivity for Furnace at 1050 °C

T = 1323 K	Field Front side $\varepsilon_{1,eff}$	Square Front side $\varepsilon_{2,eff}$	Backside $\varepsilon_{3,eff}$
Bulk p-Wafer	0.713	0.687	0.706
Epitaxial Wafer	0.713	0.689	0.806
SOI Wafer	0.665	0.786	0.706

The effective absorptivity is similarly calculated and shown in Table 3.11.

Table 3.11 Calculated Effective Absorptivity for Furnace Process (Front side) at 1250°C

T = 1523 K	Field Front side $\alpha_{FT1,eff}$	Square Front side $\alpha_{FT2,eff}$
Bulk p-Wafer	0.683	0.687
Epitaxial Wafer	0.683	0.689
SOI Wafer	0.633	0.766

The backside effective absorptivity is shown in Table 3.12.

Table 3.12 Calculated Effective Absorptivity for Furnace Process (Backside) at 850 °C

T = 1123 K	Backside $\alpha_{FB3,eff}$
Bulk p-Wafer	0.708
Epitaxial Wafer	0.795
SOI Wafer	0.708

In a lamp process, the wafer is only heated from the front side with a temperature of 2650 K. Further, it is assumed that the wafer temperature on the front side and backside are the same. A chamber reflection coefficient of 0.504 was used. The calculated effective emissivity and absorptivity are shown in Tables 3.13 and 3.14.

Table 3.13 Calculated Effective Emissivity for Lamp Heating at 1050 °C

T = 1323 K	Field Front side $\varepsilon_{1,eff}$	Square Front side $\varepsilon_{2,eff}$	Backside $\varepsilon_{3,eff}$
Bulk p-Wafer	0.772	0.749	0.671
Epitaxial Wafer	0.772	0.750	0.779
SOI Wafer	0.730	0.832	0.671

Table 3.14 Calculated Effective Absorptivity for Lamp System at 2377 °C

T = 2650 K	Field Front side $\alpha_{L1,eff}$	Square Front side $\alpha_{L2,eff}$	Backside $\alpha_{L3,eff}$
Bulk p-Wafer	0.634	0.751	0.654
Epitaxial Wafer	0.634	0.757	0.762
SOI Wafer	0.601	0.668	0.654

These values can be used in Equation 2.43 to calculate the ratio of temperature T_1 to T_2. This ratio can be compared with the experiment and used for determining the Fourier coefficients discussed in Section 2.4 and in Appendix A.

CHAPTER 4

RESULTS AND DISCUSSION

Two experiments were conducted, using RTP with open loop on unpatterned wafers and closed loop on patterned wafers. The open loop experiment, in which the lamp power was controlled, shows that emissiviy variations among the wafers produce process and temperature variations. The second experiment used patterned wafers in which temperature was maintained under closed loop control.

The model for the effect of emissivity patterns on wafer temperature, presented in Section 2, was found to give a good agreement with the experiment described in Section 3. Tables 4.1 and 4.2 show the results obtained from the model and from the closed loop temperature control experiment, respectively. The T_1/T_2 is the ratio between the absolute temperature at the origin, i.e. the square, and that at the point 4 in Figure 2.14 (T_1 and T_2 are in Kelvin).

Table 4.1 Model Calculated Temperature Ratios

	Wafer	T_1/T_2
Furnace Process	Bulk p-Wafer	0.977
	Epitaxial Wafer	0.978
	SOI Wafer	0.959
Lamp Process	Bulk p-Wafer	0.831
	Epitaxial Wafer	0.826
	SOI Wafer	0.966

Table 4.2 Temperature Ratios based on Experiments

	Wafer	T_1/T_2
Furnace Process	Bulk p-Wafer	0.987
	Epitaxial Wafer	0.987
	SOI Wafer	0.948
Lamp Process	Bulk p-Wafer	0.847
	Epitaxial Wafer	0.842
	SOI Wafer	0.946

Comparing Tables 4.1 with 4.2, a good agreement between the model and the experiment can be noted. A value for T_1/T_2 of unity can be interpreted as absolute uniform temperature distribution across the wafer and thus, a uniform process for the specific wafer. In all cases, $T_1 < T_2$, since square areas 1 with the oxide film heat more efficiently than the field areas 2 with the poly/oxide film. This is quantitatively suggested by inspection of the emissivities and absorptivities shown in Tables 3.10 – 3.14.

It is observed that the epitaxial wafers and the bulk wafers produce similar temperature non-uniformities across the wafer. In the furnace process, the experiment gives a temperature non-uniformity of $T_1/T_2 = 0.987$ for bulk and epitaxial wafer, whereas for the model, the calculated values are 0.977 and 0.978, respectively. The lamp process shows for both, bulk and epitaxial wafer, more temperature non-uniformity across the wafer than for the furnace process. This can be seen by comparing $T_1/T_2 \sim 0.8$ in the lamp system for both wafers with ~ 0.9 in the furnace system for both wafers. It can be inferred that the furnace process is more uniform for bulk and epitaxial wafers.

However, it has to be considered that the lamp system is a single side heater, whereas, in the furnace, the heat radiation is incident on both sides. For the SOI wafers, both the processes, furnace and lamp, produce comparable results. These wafers also show a good agreement in T_1/T_2 between the model (0.959 for furnace and 0.966 for lamp) and the experiment (0.948 for furnace and 0.946 for lamp).

It should be recognized that the optical properties of polysilicon and epitaxial silicon were approximated within the model. For polysilicon and epitaxial silicon, the properties of crystalline silicon were used in calculating emissivity with Multi-Rad. Another simplification relates to neglecting temperature dependence of optical properties of materials other than silicon. For SiO_2, for example, the n and k functions are taken to be temperature independent. The calculations in Multi-Rad can be very time consuming, approximately 30 minutes per wafer, and the program produces interpolation errors.

In the model, the fields and squares do not interact with one another, i.e., field and square are treated as separate wafers. In reality, the emission from field gets reflected in the chamber walls and therefore, influences the square, as well as vice versa. A further improvement of the model would be to include a different reflectivity and/or calculate the reflectivity of the wafer by using Multi-Rad. Further, the wafer is considered as an infinite plane. The higher emissivity at the edges, which also influences the temperature uniformity, is neglected. For RTP systems, steady state is not always a given. As the processing time gets shorter and the thermal budget is reduced, the steady state is less possible. A further improvement of the model would be to include the transient heating and cooling. The model is only a two-dimensional model, even though heat diffuses in

three dimensions. Since the wafer is very thin, the steady state approximation is justifiable in the present case.

A perfectly uniform temperature profile is achieved only when, for all parts of a wafer, the primary radiation flux and the reabsorbed heat radiation are balanced. Several attempts to solve this problem are given in the literature. A synergy between the temperature distribution and energy loss is necessary. One of the problems in obtaining uniform temperature profiles across a wafer surface originates from the fact that one starts with a non-uniform primary radiant flux. Even in the ideal case, the radiation from the wafer is not uniform, because of center-to-edge radiative differences and local differences in absorption and emissivity induced by patterns on the wafers. Reradiation back onto the wafer enhances these differences [19].

It is evident that a reflective chamber reduces the effective energy loss, and thus the pattern-induced non-uniformity. By changing the method of illumination, the effect of patterns on the temperature non-uniformity can either be amplified or reduced, e.g. double side heating or single sided heating. To suppress non-uniformities during steady state, it is best to illuminate only the unpatterned side during the ramping stage and to compensate the energy loss during stationary state by double-sided heating. Dynamic non-uniformity can be reduced by increasing the contribution of backside heating with respect to front side heating. Here it is clear that transient non-uniformity is also suppressed by increasing ramp-up times [20].

Some RTP chambers also rotate the wafer in order to get a uniform temperature distribution. Modeling a rotating wafer will be more challenging since there is a time dependence.

Experimental results from the literature also demonstrate the possibility of pattern-effect minimization using a hot shielding wafer [20]. Kersch [21] showed in his paper, that there is no pattern effect when using a susceptor to control the wafer temperature in a single wafer reactor. The wafer was oriented towards the susceptor and the wafer and susceptor had the same temperature. There was a minimal effect because the configuration is not ideal: There is some radiation entering from the side [21].

The influence of the deposition system and patterns on the thickness uniformity can be further reduced by choosing an optimum chemistry. Processes with lower activation energies will result in better process uniformities.

Furthermore, it is important to point out that not only the lateral but also the vertical temperature gradient can be a decisive factor. Given the case of front side heating, limited thermal conductivity and interference on the patterned layer at the wafer surface creates a temperature gradient vertically across the wafer.

In the experiment, the furnace was a heat source in which the wafer was heated from both sides. This can be compared to the lamp system, i.e., a single sided heating system. The experiments reported in this study show that the temperature difference in the furnace system is smaller than in the lamp system.

APPENDIX A

DERIVATION OF THE HEAT BALANCE EQUATION

In this appendix, the derivation of the heat balance equation of a squared patterned wafer in two dimensions is derived by using Fourier analysis.

The heat balance equation and the general 3 D Fourier heat conduction equation is used to describe the temperature profile within a heated wafer. The thermal diffusion equation is given as:

$$\rho C \frac{\partial T}{\partial t} = \lambda(T) t_w \nabla^2 T + \dot{q} \tag{A.1}$$

In A.1 ρ is the density of the material, C the specific heat of the solid and $\dot{q}$ the heat flow. The density is assumed to be homogenous. In a solid, there is negligible difference between the specific heat at a constant volume c_v and a constant pressure c_p. $\lambda(T)$ and t_w is the thermal conductivity and wafer thickness, respectively. The heat flow in this case is the difference of the heat absorbed (heat source) and the heat emitted (heat loss). For 1 dimension:

$$\lambda(T) t_w \frac{\partial^2 T(x,t)}{\partial x^2} + q_{abs}(x,T) - 2\varepsilon(x,T)\sigma T(x,t)^4 = \rho C t_w \frac{\partial T(x,t)}{\partial t} \tag{A.2}$$

In A.2, the variable x is the position, T the temperature and t the time. The first term expresses the thermal conduction in the wafer. The thermal conductivity is temperature dependent. $\lambda(T)$ is the thermal conductivity and t_w the thickness of the wafer. To the thermal conduction, the heat absorbed at the position x is added. The absorbed heat energy density $q_{abs}(x,T)$ is obtained using the following equation:

$$q_{abs}(T,x) = Q(T)\alpha(x) \tag{A.3}$$

79

where, Q(T) is the heat input power and is defined by the Stefan-Boltzmann law and $\alpha(x)$ is the absorption coefficient at the point x. The heat loss is defined through the emissivity. This differential equation can be solved analytically. Taking a closer look at the solution, the thermal diffusion length can be expressed as:

$$L_d = \sqrt{\frac{\lambda t_w}{8\varepsilon\sigma T^3}}$$ (A.4)

Equation A.2 also can be extended to two dimensions. A two-dimensional pattern function is superposed with the emissivity and absorptivity. This two-dimensional pattern function is realized with a two-dimensional Fourier square wave series. This series is centered in the square, i.e. it is a symmetrical square wave, with an offset to avoid negative emissivties and absorptivities.

$$U(x) = \sum_{n=1,3\ldots} f_n \sin(k_n x)$$ (A.5)

Equation A.5 is a one-dimensional square wave Fourier series with the Fourier coefficient $f_n = \frac{4}{\pi n}$ and $k_n = \frac{4}{\pi n}$. This function is made symmetrical about the origin by shifting x by $\frac{L}{2}$. This introduces a phase factor.

$$S(x) = U\left(x + \frac{L}{2}\right) = \sum_{n=1,3\ldots} (-1)^{\frac{n-1}{2}} f_n \cos(k_n x)$$ (A.6)

The pattern is an offset symmetrical square wave, hence Equation A.6 becomes:

$$F(x) = \frac{1 + S(x)}{2}$$ (A.7)

A two-dimensional pattern function is created by multiplying a one dimensional pattern function F(x) with a pattern function F(y).

$$P(x,y) = \frac{1}{4} + \sum_{n=1,3,...} \frac{1}{\pi n}(-1)^{\frac{n-1}{2}} \cos(k_n x) + \sum_{n=1,3,...} \frac{1}{\pi n}(-1)^{\frac{n-1}{2}} \cos(k_n y) + \frac{1}{4}\sum_{n=1,3,...} \frac{4}{\pi n}(-1)^{\frac{n-1}{2}} \cos(k_n x) \sum_{n=1,3,...} \frac{4}{\pi n}(-1)^{\frac{n-1}{2}} \cos(k_n y) \quad (A.8)$$

The heat balance equation is simplified with the approximation $T(x,y) = T_0 + \Delta T(x,y)$, where, $\Delta T(x,y) \ll T_0$:

$$0 = \lambda(T)t_w \nabla^2 \Delta T(x,y) + q_{abs}(x,y,T) - 2\varepsilon(x,y,T)\sigma T_0^4 - 8T_0^3 \varepsilon(x,y,T)\sigma \Delta T(x,y) \quad (A.9)$$

Simplification of the heat balance equation leads to:

$$\lambda(T)t_w \nabla^2 \Delta T(x,y) + q_{abs}(x,y,T) - 2\varepsilon(x,y,T)\sigma T_0^4 - 8T_0^3 \varepsilon(x,y,T)\sigma \Delta T(x,y)$$

$$\lambda(T)t_w \nabla^2 T_0 + \lambda(T)t_w \nabla^2 \Delta T(x,y) + Q(T)\alpha_0 + Q(T)(\alpha_1 - \alpha_0)P(x,y) - 2\varepsilon_0 \sigma T_0^4 - 2P(x,y)(\varepsilon_1 - \varepsilon_0)\sigma T_0^4$$
$$- 8T_0^4 \varepsilon_0 \sigma - 8T_0^3 \varepsilon_0 \Delta T(x,y) - 8T_0^4 P(x,y)(\varepsilon_1 - \varepsilon_0)\sigma - 8T_0^3 P(x,y)(\varepsilon_1 - \varepsilon_0)\sigma \Delta T(x,y)$$

Since T_0 is a constant, the first term is zero: $\lambda(T)t_w \nabla^2 T_0 = \lambda(T)t_w \left(\frac{\partial^2}{\partial x^2} + \frac{\partial^2}{\partial y^2}\right)T_0 = 0$

And considering only x and y dependence, the result can be simplified further:

$$c_1 \nabla^2 \Delta T(x,y) + c_3 + c_4 P(x,y) - c_5 - c_6 P(x,y) - c_7 - c_8 \Delta T(x,y) - c_9 P(x,y) - c_{10} P(x,y)\Delta T(x,y)$$

There are five different terms, terms without any xy dependence, terms with $\nabla^2 \Delta T(x,y)$, $P(x,y)$, $\Delta T(x,y)$ and $P(x,y)*\Delta T(x,y)$ dependence. Therefore, it is possible to combine certain constants:

$$c^* = c_3 - c_5 - c_7$$

$$c^{**} = c_4 - c_6 - c_9$$

$$c_1 \nabla^2 \Delta T(x,y) - c_{10} P(x,y)\Delta T(x,y) + c^{**} P(x,y) - c_8 \Delta T(x,y) + c^* \quad (A.10)$$

As an approach to solve equation A.10, for $\Delta T(x,y)$ the general Fourier series formula is used.

$$\Delta T(x,y) = \frac{1}{4}\left[\begin{array}{l} 1 + \sum_{n=1,3,\ldots} t_n(-1)^{\frac{n-1}{2}}\cos(k_n x) + \sum_{n=1,3,\ldots} t_n(-1)^{\frac{n-1}{2}}\cos(k_n y) \\ + \sum_{n=1,3,\ldots} t_n(-1)^{\frac{n-1}{2}}\cos(k_n x)\sum_{n=1,3,\ldots} t_n(-1)^{\frac{n-1}{2}}\cos(k_n y) \end{array}\right] \qquad (A.11)$$

The first term is:

$$\nabla^2 \Delta T(x,y) = \left(\frac{\partial^2}{\partial x^2} + \frac{\partial^2}{\partial y^2}\right)\Delta T(x,y)$$

$$\frac{\partial^2}{\partial x^2}\Delta T(x,y) = \frac{1}{4}\left[\begin{array}{l} 0 - \sum_{n=1,3,\ldots} t_n(-1)^{\frac{n-1}{2}} k_n^2\cos(k_n x) + 0 \\ - \sum_{n=1,3,\ldots} t_n(-1)^{\frac{n-1}{2}} k_n^2\cos(k_n x)\sum_{n=1,3,\ldots} t_n(-1)^{\frac{n-1}{2}}\cos(k_n y) \end{array}\right]$$

$$\frac{\partial^2}{\partial y^2}\Delta T(x,y) = \frac{1}{4}\left[\begin{array}{l} 0 + 0 - \sum_{n=1,3,\ldots} t_n(-1)^{\frac{n-1}{2}} k_n^2\cos(k_n y) \\ - \sum_{n=1,3,\ldots} t_n(-1)^{\frac{n-1}{2}}\cos(k_n x)\sum_{n=1,3,\ldots} t_n(-1)^{\frac{n-1}{2}} k_n^2\cos(k_n y) \end{array}\right]$$

$$\nabla^2 \Delta T(x,y) = -\frac{1}{4}\sum_{n=1,3,\ldots} t_n(-1)^{\frac{n-1}{2}} k_n^2\cos(k_n x) - \frac{1}{4}\sum_{n=1,3,\ldots} t_n(-1)^{\frac{n-1}{2}} k_n^2\cos(k_n y)$$

$$-\frac{1}{4}\sum_{n=1,3,\ldots} t_n(-1)^{\frac{n-1}{2}} k_n^2\cos(k_n x)\sum_{n=1,3,\ldots} t_n(-1)^{\frac{n-1}{2}}\cos(k_n y)$$

$$-\frac{1}{4}\sum_{n=1,3,\ldots} t_n(-1)^{\frac{n-1}{2}}\cos(k_n x)\sum_{n=1,3,\ldots} t_n(-1)^{\frac{n-1}{2}} k_n^2\cos(k_n y)$$

For $P(x,y)\Delta T(x,y)$:

$$P(x,y)\Delta T(x,y)$$

$$=\frac{1}{16}+\frac{1}{16}\sum_{n=1,3,...}t_n(-1)^{\frac{n-1}{2}}\cos(k_nx)+\frac{1}{16}\sum_{n=1,3,...}t_n(-1)^{\frac{n-1}{2}}\cos(k_ny)$$

$$+\frac{1}{16}\sum_{n=1,3,...}t_n(-1)^{\frac{n-1}{2}}\cos(k_nx)\sum_{n=1,3,...}t_n(-1)^{\frac{n-1}{2}}\cos(k_ny)$$

$$+\frac{1}{4}\sum_{n=1,3,...}\frac{1}{\pi n}(-1)^{\frac{n-1}{2}}\cos(k_nx)+\frac{1}{4}\sum_{n=1,3,...}\frac{1}{\pi n}(-1)^{\frac{n-1}{2}}\cos(k_nx)\sum_{n=1,3,...}t_n(-1)^{\frac{n-1}{2}}\cos(k_nx)$$

$$+\frac{1}{4}\sum_{n=1,3,...}\frac{1}{\pi n}(-1)^{\frac{n-1}{2}}\cos(k_nx)\sum_{n=1,3,...}t_n(-1)^{\frac{n-1}{2}}\cos(k_ny)$$

$$+\frac{1}{4}\sum_{n=1,3,...}\frac{1}{\pi n}(-1)^{\frac{n-1}{2}}\cos(k_nx)\sum_{n=1,3,...}t_n(-1)^{\frac{n-1}{2}}\cos(k_nx)\sum_{n=1,3,...}t_n(-1)^{\frac{n-1}{2}}\cos(k_ny)$$

$$+\frac{1}{4}\sum_{n=1,3,...}\frac{1}{\pi n}(-1)^{\frac{n-1}{2}}\cos(k_ny)+\frac{1}{4}\sum_{n=1,3,...}\frac{1}{\pi n}(-1)^{\frac{n-1}{2}}\cos(k_ny)\sum_{n=1,3,...}t_n(-1)^{\frac{n-1}{2}}\cos(k_nx)$$

$$+\frac{1}{4}\sum_{n=1,3,...}\frac{1}{\pi n}(-1)^{\frac{n-1}{2}}\cos(k_ny)\sum_{n=1,3,...}t_n(-1)^{\frac{n-1}{2}}\cos(k_ny)$$

$$+\frac{1}{4}\sum_{n=1,3,...}\frac{1}{\pi n}(-1)^{\frac{n-1}{2}}\cos(k_ny)\sum_{n=1,3,...}t_n(-1)^{\frac{n-1}{2}}\cos(k_nx)\sum_{n=1,3,...}t_n(-1)^{\frac{n-1}{2}}\cos(k_ny)$$

$$+\frac{1}{16}\sum_{n=1,3,...}\frac{1}{\pi n}(-1)^{\frac{n-1}{2}}\cos(k_nx)\sum_{n=1,3,...}\frac{1}{\pi n}(-1)^{\frac{n-1}{2}}\cos(k_ny)$$

$$+\frac{1}{16}\sum_{n=1,3,...}\frac{1}{\pi n}(-1)^{\frac{n-1}{2}}\cos(k_nx)\sum_{n=1,3,...}\frac{1}{\pi n}(-1)^{\frac{n-1}{2}}\cos(k_ny)\sum_{n=1,3,...}t_n(-1)^{\frac{n-1}{2}}\cos(k_nx)$$

$$+\frac{1}{16}\sum_{n=1,3,...}\frac{1}{\pi n}(-1)^{\frac{n-1}{2}}\cos(k_nx)\sum_{n=1,3,...}\frac{1}{\pi n}(-1)^{\frac{n-1}{2}}\cos(k_ny)\sum_{n=1,3,...}t_n(-1)^{\frac{n-1}{2}}\cos(k_ny)$$

$$+\frac{1}{16}\sum_{n=1,3,...}\frac{1}{\pi n}(-1)^{\frac{n-1}{2}}\cos(k_nx)\sum_{n=1,3,...}\frac{1}{\pi n}(-1)^{\frac{n-1}{2}}\cos(k_ny)\sum_{n=1,3,...}t_n(-1)^{\frac{n-1}{2}}\cos(k_nx)\sum_{n=1,3,...}t_n(-1)^{\frac{n-1}{2}}\cos(k_ny)$$

Going back to Equation A.10:

$$c_1 \nabla^2 \Delta T(x,y) - c_{10} P(x,y) \Delta T(x,y) + c^{**} P(x,y) - c_8 \Delta T(x,y) + c^*$$

$$= -c_1 \frac{1}{4} \sum_{n=1,3,\ldots} t_n (-1)^{\frac{n-1}{2}} k_n^2 \cos(k_n x) - c_1 \frac{1}{4} \sum_{n=1,3,\ldots} t_n (-1)^{\frac{n-1}{2}} k_n^2 \cos(k_n y) - c_1 \frac{1}{4} \sum_{n=1,3,\ldots} t_n (-1)^{\frac{n-1}{2}} k_n^2 \cos(k_n x) \sum t_n (-1)^{\frac{n-1}{2}} \cos(k_n y)$$

$$-c_1 \frac{1}{4} \sum_{n=1,3,\ldots} t_n (-1)^{\frac{n-1}{2}} \cos(k_n x) \sum_{n=1,3,\ldots} t_n (-1)^{\frac{n-1}{2}} k_n^2 \cos(k_n y) - c_{10} \frac{1}{16} - c_{10} \frac{1}{16} \sum_{n=1,3,\ldots} t_n (-1)^{\frac{n-1}{2}} \cos(k_n x) - c_{10} \frac{1}{16} \sum_{n=1,3,\ldots} t_n (-1)^{\frac{n-1}{2}} \cos(k_n y)$$

$$-c_{10} \frac{1}{16} \sum_{n=1,3,\ldots} t_n (-1)^{\frac{n-1}{2}} \cos(k_n x) \sum_{n=1,3,\ldots} t_n (-1)^{\frac{n-1}{2}} \cos(k_n y) - c_{10} \frac{1}{4} \sum_{n=1,3,\ldots} \frac{1}{\pi n} (-1)^{\frac{n-1}{2}} \cos(k_n x)$$

$$-c_{10} \frac{1}{4} \sum_{n=1,3,\ldots} \frac{1}{\pi n} (-1)^{\frac{n-1}{2}} \cos(k_n x) \sum_{n=1,3,\ldots} t_n (-1)^{\frac{n-1}{2}} \cos(k_n x) - c_{10} \frac{1}{4} \sum_{n=1,3,\ldots} \frac{1}{\pi n} (-1)^{\frac{n-1}{2}} \cos(k_n x) \sum_{n=1,3,\ldots} t_n (-1)^{\frac{n-1}{2}} \cos(k_n y)$$

$$-c_{10} \frac{1}{4} \sum_{n=1,3,\ldots} \frac{1}{\pi n} (-1)^{\frac{n-1}{2}} \cos(k_n x) \sum_{n=1,3,\ldots} t_n (-1)^{\frac{n-1}{2}} \cos(k_n x) \sum_{n=1,3,\ldots} t_n (-1)^{\frac{n-1}{2}} \cos(k_n y)$$

$$-c_{10} \frac{1}{4} \sum_{n=1,3,\ldots} \frac{1}{\pi n} (-1)^{\frac{n-1}{2}} \cos(k_n y) - c_{10} \frac{1}{4} \sum_{n=1,3,\ldots} \frac{1}{\pi n} (-1)^{\frac{n-1}{2}} \cos(k_n y) \sum_{n=1,3,\ldots} t_n (-1)^{\frac{n-1}{2}} \cos(k_n x)$$

$$-c_{10} \frac{1}{4} \sum_{n=1,3,\ldots} \frac{1}{\pi n} (-1)^{\frac{n-1}{2}} \cos(k_n y) \sum_{n=1,3,\ldots} t_n (-1)^{\frac{n-1}{2}} \cos(k_n y)$$

$$-c_{10} \frac{1}{4} \sum_{n=1,3,\ldots} \frac{1}{\pi n} (-1)^{\frac{n-1}{2}} \cos(k_n y) \sum_{n=1,3,\ldots} t_n (-1)^{\frac{n-1}{2}} \cos(k_n x) \sum_{n=1,3,\ldots} t_n (-1)^{\frac{n-1}{2}} \cos(k_n y)$$

$$-c_{10} \frac{1}{16} \sum_{n=1,3,\ldots} \frac{1}{\pi n} (-1)^{\frac{n-1}{2}} \cos(k_n x) \sum_{n=1,3,\ldots} \frac{1}{\pi n} (-1)^{\frac{n-1}{2}} \cos(k_n y)$$

$$-c_{10} \frac{1}{16} \sum_{n=1,3,\ldots} \frac{1}{\pi n} (-1)^{\frac{n-1}{2}} \cos(k_n x) \sum_{n=1,3,\ldots} \frac{1}{\pi n} (-1)^{\frac{n-1}{2}} \cos(k_n y) \sum_{n=1,3,\ldots} t_n (-1)^{\frac{n-1}{2}} \cos(k_n x)$$

$$-c_{10} \frac{1}{16} \sum_{n=1,3,\ldots} \frac{1}{\pi n} (-1)^{\frac{n-1}{2}} \cos(k_n x) \sum_{n=1,3,\ldots} \frac{1}{\pi n} (-1)^{\frac{n-1}{2}} \cos(k_n y) \sum_{n=1,3,\ldots} t_n (-1)^{\frac{n-1}{2}} \cos(k_n y)$$

$$-c_{10} \frac{1}{16} \sum_{n=1,3,\ldots} \frac{1}{\pi n} (-1)^{\frac{n-1}{2}} \cos(k_n x) \sum_{n=1,3,\ldots} \frac{1}{\pi n} (-1)^{\frac{n-1}{2}} \cos(k_n y) \sum_{n=1,3,\ldots} t_n (-1)^{\frac{n-1}{2}} \cos(k_n x) \sum_{n=1,3,\ldots} t_n (-1)^{\frac{n-1}{2}} \cos(k_n y)$$

$$+c^{**} \frac{1}{4} + c^{**} \sum_{n=1,3,\ldots} \frac{1}{\pi n} (-1)^{\frac{n-1}{2}} \cos(k_n x) + c^{**} \sum_{n=1,3,\ldots} \frac{1}{\pi n} (-1)^{\frac{n-1}{2}} \cos(k_n y) + c^{**} \frac{1}{4} \sum_{n=1,3,\ldots} \frac{4}{\pi n} (-1)^{\frac{n-1}{2}} \cos(k_n x) \sum_{n=1,3,\ldots} \frac{4}{\pi n} (-1)^{\frac{n-1}{2}} \cos(k_n y)$$

$$-c_8 \frac{1}{4} - c_8 \frac{1}{4} \sum_{n=1,3,\ldots} t_n (-1)^{\frac{n-1}{2}} \cos(k_n x) - c_8 \frac{1}{4} \sum_{n=1,3,\ldots} t_n (-1)^{\frac{n-1}{2}} \cos(k_n y) - c_8 \frac{1}{4} \sum_{n=1,3,\ldots} t_n (-1)^{\frac{n-1}{2}} \cos(k_n x) \sum_{n=1,3,\ldots} t_n (-1)^{\frac{n-1}{2}} \cos(k_n y) + c^*$$

Both coordinates are independent; hence we consider first the x coordinate.

$$= -c_1 \iint \frac{1}{4} t_n (-1)^{\frac{n-1}{2}} k_n^2 \cos^2(k_n x) dx dy - c_{10} \iint \frac{1}{16} t_n (-1)^{\frac{n-1}{2}} \cos^2(k_n x) dx dy - c_{10} \iint \frac{1}{4} \frac{1}{\pi n} (-1)^{\frac{n-1}{2}} \cos^2(k_n x) dx dy$$

$$- c_{10} \iint \frac{1}{4} \frac{1}{\pi n} (-1)^{\frac{n-1}{2}} \cos(k_n y) t_n (-1)^{\frac{n-1}{2}} \cos(k_n x)^2 t_n (-1)^{\frac{n-1}{2}} \cos(k_n y) dx dy$$

$$- c_{10} \iint \frac{1}{16} \frac{1}{\pi n} (-1)^{\frac{n-1}{2}} \cos^2(k_n x) \frac{1}{\pi n} (-1)^{\frac{n-1}{2}} \cos(k_n y) t_n (-1)^{\frac{n-1}{2}} \cos(k_n y) dx dy$$

$$+ c^{**} \iint \frac{1}{\pi n} (-1)^{\frac{n-1}{2}} \cos(k_n x)^2 dx dy - c_8 \frac{1}{4} \iint t_n (-1)^{\frac{n-1}{2}} \cos^2(k_n x) dx dy$$

$$= -c_1 \frac{1}{4} t_n (-1)^{\frac{n-1}{2}} k_n^2 \left(\frac{x}{2} + \frac{\sin(2k_n x)}{4k_n} \right) y - c_{10} \frac{1}{16} t_n (-1)^{\frac{n-1}{2}} \left(\frac{x}{2} + \frac{\sin(2k_n x)}{4k_n} \right) y - c_{10} \frac{1}{4} \frac{1}{\pi n} (-1)^{\frac{n-1}{2}} \left(\frac{x}{2} + \frac{\sin(2k_n x)}{4k_n} \right) y$$

$$- c_{10} \frac{1}{4} \frac{1}{\pi n} (-1)^{\frac{n-1}{2}} t_n (-1)^{\frac{n-1}{2}} t_n (-1)^{\frac{n-1}{2}} \left(\frac{x}{2} + \frac{\sin(2k_n x)}{4k_n} \right) \left(\frac{y}{2} + \frac{\sin(2k_n y)}{4k_n} \right)$$

$$- c_{10} \frac{1}{16} \frac{1}{\pi n} (-1)^{\frac{n-1}{2}} \frac{1}{\pi n} (-1)^{\frac{n-1}{2}} t_n (-1)^{\frac{n-1}{2}} \left(\frac{x}{2} + \frac{\sin(2k_n x)}{4k_n} \right) \left(\frac{y}{2} + \frac{\sin(2k_n y)}{4k_n} \right)$$

$$+ c^{**} \frac{1}{\pi n} (-1)^{\frac{n-1}{2}} \left(\frac{x}{2} + \frac{\sin(2k_n x)}{4k_n} \right) y - c_8 \frac{1}{4} t_n (-1)^{\frac{n-1}{2}} \left(\frac{x}{2} + \frac{\sin(2k_n x)}{4k_n} \right) y$$

$$= -c_1 \frac{1}{4} t_n (-1)^{\frac{n-1}{2}} k_n^2 \left(\frac{L}{2} \right) L - c_{10} \frac{1}{16} t_n (-1)^{\frac{n-1}{2}} \left(\frac{L}{2} \right) L - c_{10} \frac{1}{4} \frac{1}{\pi n} (-1)^{\frac{n-1}{2}} \left(\frac{L}{2} \right) L$$

$$- c_{10} \frac{1}{4} \frac{1}{\pi n} (-1)^{\frac{n-1}{2}} t_n (-1)^{\frac{n-1}{2}} t_n (-1)^{\frac{n-1}{2}} \left(\frac{L}{2} \right) \left(\frac{L}{2} \right)$$

$$- c_{10} \frac{1}{16} \frac{1}{\pi n} (-1)^{\frac{n-1}{2}} \frac{1}{\pi n} (-1)^{\frac{n-1}{2}} t_n (-1)^{\frac{n-1}{2}} \left(\frac{L}{2} \right) \left(\frac{L}{2} \right)$$

$$+ c^{**} \frac{1}{\pi n} (-1)^{\frac{n-1}{2}} \left(\frac{L}{4} \right) \frac{L}{2} - c_8 \frac{1}{4} t_n (-1)^{\frac{n-1}{2}} \left(\frac{L}{2} \right) L$$

$$= -c_1 \frac{1}{8} t_n (-1)^{\frac{n-1}{2}} k_n^2 L^2 - c_{10} \frac{1}{32} t_n (-1)^{\frac{n-1}{2}} L^2 - c_{10} \frac{1}{8} \frac{1}{\pi n} (-1)^{\frac{n-1}{2}} L^2 - c_{10} \frac{1}{16} \frac{1}{\pi n} (-1)^{\left(\frac{n-1}{2} \right)} t_n^2 L^2$$

$$- c_{10} \frac{1}{64} \frac{1}{\pi^2 n^2} (-1)^{3 \left(\frac{n-1}{2} \right)} t_n L^2 + c^{**} \frac{1}{4} \frac{1}{\pi n} (-1)^{\frac{n-1}{2}} L^2 - c_8 \frac{1}{8} t_n (-1)^{\frac{n-1}{2}} L^2$$

$$0 = -c_1 \frac{1}{8} t_n (-1)^{\frac{n-1}{2}} k_n^2 - c_{10} \frac{1}{32} t_n (-1)^{\frac{n-1}{2}} - c_{10} \frac{1}{8} \frac{1}{\pi n} (-1)^{\frac{n-1}{2}} - c_{10} \frac{1}{16} \frac{1}{\pi n} (-1)^{3\left(\frac{n-1}{2}\right)} t_n^2 - c_{10} \frac{1}{64} \frac{1}{\pi^2 n^2} (-1)^{3\left(\frac{n-1}{2}\right)} t_n + c^{**} \frac{1}{4} \frac{1}{\pi n} (-1)^{\frac{n-1}{2}} - c_8 \frac{1}{8} t_n (-1)^{\frac{n-1}{2}}$$

$$0 = -c_1 \frac{1}{2} t_n (-1)^{\frac{n-1}{2}} k_n^2 - c_{10} \frac{1}{8} t_n (-1)^{\frac{n-1}{2}} - c_{10} \frac{1}{2} \frac{1}{\pi n} (-1)^{\frac{n-1}{2}} - c_{10} \frac{1}{4} \frac{1}{\pi n} (-1)^{3\left(\frac{n-1}{2}\right)} t_n^2 - c_{10} \frac{1}{16} \frac{1}{\pi^2 n^2} (-1)^{3\left(\frac{n-1}{2}\right)} t_n + c^{**} \frac{1}{\pi n} (-1)^{\frac{n-1}{2}} - c_8 \frac{1}{2} t_n (-1)^{\frac{n-1}{2}}$$

$$0 = -c_{10} \frac{1}{4} \frac{1}{\pi n} (-1)^{3\left(\frac{n-1}{2}\right)} t_n^2 - \left(c_1 \frac{1}{2} (-1)^{\frac{n-1}{2}} k_n^2 + c_{10} \frac{1}{8} (-1)^{\frac{n-1}{2}} + c_{10} \frac{1}{16} \frac{1}{\pi^2 n^2} (-1)^{3\left(\frac{n-1}{2}\right)} + c_8 \frac{1}{2} (-1)^{\frac{n-1}{2}} \right) t_n - c_{10} \frac{1}{2} \frac{1}{\pi n} (-1)^{\frac{n-1}{2}} + c^{**} \frac{1}{\pi n} (-1)^{\frac{n-1}{2}}$$

$$0 = -c_{10} \frac{1}{4} \frac{1}{\pi n} (-1)^{3\left(\frac{n-1}{2}\right)} t_n^2 - \left(\frac{1}{2} (-1)^{\frac{n-1}{2}} \left(c_1 k_n^2 + c_{10} \frac{1}{4} + c_8 \right) + c_{10} \frac{1}{16} \frac{1}{\pi^2 n^2} (-1)^{3\left(\frac{n-1}{2}\right)} \right) t_n - c_{10} \frac{1}{2} \frac{1}{\pi n} (-1)^{\frac{n-1}{2}} + c^{**} \frac{1}{\pi n} (-1)^{\frac{n-1}{2}}$$

$$0 = -c_{10} \frac{1}{4} \frac{1}{\pi n} (-1)^{n-1} t_n^2 - \left(\frac{1}{2} \left(c_1 k_n^2 + c_{10} \frac{1}{4} + c_8 \right) + c_{10} \frac{1}{16} \frac{1}{\pi^2 n^2} (-1)^{n-1} \right) t_n + \left(c^{**} - \frac{1}{2} c_{10} \right) \frac{1}{\pi n}$$

$$t_{n1/2} = \frac{\frac{1}{2} \left(c_1 k_n^2 + c_{10} \frac{1}{4} + c_8 \right) + c_{10} \frac{1}{16} \frac{1}{\pi^2 n^2} (-1)^{n-1} \pm \sqrt{ \left(-\frac{1}{2} \left(c_1 k_n^2 + c_{10} \frac{1}{4} + c_8 \right) - c_{10} \frac{1}{16} \frac{1}{\pi^2 n^2} (-1)^{n-1} \right)^2 - 4 \left(-c_{10} \frac{1}{4} \frac{1}{\pi n} (-1)^{n-1} \right) \left(\left(c^{**} - \frac{1}{2} c_{10} \right) \frac{1}{\pi n} \right) }}{-2 c_{10} \frac{1}{4} \frac{1}{\pi n} (-1)^{n-1}}$$

$$t_{n1/2} = \frac{\frac{1}{2} \left(c_1 k_n^2 + c_{10} \frac{1}{4} + c_8 \right) + c_{10} \frac{1}{16} \frac{1}{\pi^2 n^2} (-1)^{n-1} \pm \sqrt{ \left(-\frac{1}{2} \left(c_1 k_n^2 + c_{10} \frac{1}{4} + c_8 \right) - c_{10} \frac{1}{16} \frac{1}{\pi^2 n^2} (-1)^{n-1} \right)^2 - \left(-c_{10} \frac{1}{\pi n} (-1)^{n-1} \right) \left(\left(c^{**} - \frac{1}{2} c_{10} \right) \frac{1}{\pi n} \right) }}{-\frac{1}{2} c_{10} \frac{1}{\pi n} (-1)^{n-1}}$$

$$t_{n1/2} = \frac{\frac{1}{2} \left(c_1 k_n^2 + c_{10} \frac{1}{4} + c_8 \right) + c_{10} \frac{1}{16} \frac{1}{\pi^2 n^2} (-1)^{n-1}}{-\frac{1}{2} c_{10} \frac{1}{\pi n} (-1)^{n-1}}$$

$$\pm \frac{\sqrt{ \frac{c_{10}}{64} + \frac{c_{10} c_8}{8} + \frac{c_8^2}{4} + \frac{1}{8} c_1 c_{10} k_n^2 + \frac{1}{2} c_1 c_8 k_n^2 + \frac{c_1^2 k_n^4}{4} + \frac{c_{10}^2 (-1)^{2n-2}}{256 \pi^4 n^4} + \frac{c_{10}^2 (-1)^{n-1}}{64 \pi^2 n^2} + \frac{c_{10} c_8 (-1)^{n-1}}{16 \pi^2 n^2} + \frac{c_{10} c_1 (-1)^{n-1} k_n^2}{16 \pi^2 n^2} - \left(-c_{10} (-1)^{n-1} c^{**} + c_{10}^2 (-1)^{n-1} \frac{1}{2} \right) \frac{1}{\pi^2 n^2} }}{-\frac{1}{2} c_{10} \frac{1}{\pi n} (-1)^{n-1}}$$

$$t_{n1/2} = \frac{\frac{1}{2}\left(c_1 k_n^2 + c_{10}\frac{1}{4} + c_8\right) + c_{10}\frac{1}{16}\frac{1}{\pi^2 n^2}(-1)^{n-1}}{-\frac{1}{2}c_{10}\frac{1}{\pi n}(-1)^{n-1}}$$

$$\pm \frac{\sqrt{\begin{aligned}&\frac{c_{10}}{64} + \frac{c_{10}c_8}{8} + \frac{c_8^2}{4} + \frac{1}{8}c_1 c_{10} k_n^2 + \frac{1}{2}c_1 c_8 k_n^2 + \frac{c_1^2 k_n^4}{4} + \frac{c_{10}^2(-1)^{2n-2}}{256\pi^4 n^4}\\ &+ \frac{c_{10}^2(-1)^{n-1}}{64\pi^2 n^2} + \frac{c_{10}c_8(-1)^{n-1}}{16\pi^2 n^2} + \frac{c_{10}c_1(-1)^{n-1}k_n^2}{16\pi^2 n^2} + c_{10}(-1)^{n-1}c^{\cdot\cdot}\frac{1}{\pi^2 n^2} - c_{10}^2(-1)^{n-1}\frac{1}{2}\frac{1}{\pi^2 n^2}\end{aligned}}}{-\frac{1}{2}c_{10}\frac{1}{\pi n}(-1)^{n-1}}$$

$$t_{n1/2} = \frac{\frac{1}{2}\left(c_1 k_n^2 + c_{10}\frac{1}{4} + c_8\right) + c_{10}\frac{1}{16}\frac{1}{\pi^2 n^2}(-1)^{n-1} \pm \sqrt{\begin{aligned}&\frac{c_{10}}{64} + \frac{c_{10}c_8}{8} + \frac{c_8^2}{4} + \frac{1}{8}c_1 c_{10} k_n^2 + \frac{1}{2}c_1 c_8 k_n^2\\ &+ \frac{c_1^2 k_n^4}{4} + \frac{c_{10}^2(-1)^{2n-2}}{256\pi^4 n^4} + \frac{c_{10}(-1)^{n-1}}{16\pi^2 n^2}\left(c_8 + c_1 k_n^2 + 16c^{\cdot\cdot} - \frac{31}{4}c_{10}\right)\end{aligned}}}{-\frac{1}{2}c_{10}\frac{1}{\pi n}(-1)^{n-1}}$$

$$t_{n1/2} = \frac{\frac{1}{2}\left(\lambda(T)t_w k_n^2 + 2T_0^3(\varepsilon_1 - \varepsilon_0)\sigma + 8T_0^3\varepsilon_0\right) + \frac{1}{2}T_0^3(\varepsilon_1 - \varepsilon_0)\sigma\frac{1}{\pi^2 n^2}(-1)^{n-1}}{-4T_0^3(\varepsilon_1 - \varepsilon_0)\sigma\frac{1}{\pi n}(-1)^{n-1}}$$

$$\pm \frac{\sqrt{\begin{aligned}&\frac{T_0^3(\varepsilon_1-\varepsilon_0)\sigma}{8} + T_0^3(\varepsilon_1-\varepsilon_0)\sigma 8T_0^3\varepsilon_0 + 16T_0^6\varepsilon_0^2 + \lambda(T)t_w T_0^3(\varepsilon_1-\varepsilon_0)\sigma k_n^2 + 4\lambda(T)t_w T_0^3\varepsilon_0 k_n^2 + \frac{\lambda^2(T)t_w^2 k_n^4}{4}\\ &+ \frac{T_0^6(\varepsilon_1-\varepsilon_0)^2\sigma^2(-1)^{2n-2}}{4\pi^4 n^4} + \frac{T_0^3(\varepsilon_1-\varepsilon_0)\sigma(-1)^{n-1}}{2\pi^2 n^2}\left(8T_0^3\varepsilon_0 + \lambda(T)t_w k_n^2 + 16(c_4 - c_6 - c_9) - 62T_0^3(\varepsilon_1-\varepsilon_0)\sigma\right)\end{aligned}}}{-4T_0^3(\varepsilon_1-\varepsilon_0)\sigma\frac{1}{\pi n}(-1)^{n-1}}$$

$$c_4 - c_6 - c_9 = Q(T)(\alpha_1 - \alpha_0) - 2(\varepsilon_1 - \varepsilon_0)\sigma T_0^4 - 8(\varepsilon_1 - \varepsilon_0)\sigma T_0^4 = Q(T)(\alpha_1 - \alpha_0) - 10(\varepsilon_1 - \varepsilon_0)\sigma T_0^4$$

$$t_{n1/2} = \cfrac{\cfrac{1}{2}\left(\lambda(T)t_w k_n^2 + 2T_0^3(\varepsilon_1 - \varepsilon_0)\sigma + 8T_0^3\varepsilon_0\right) + \cfrac{1}{2}T_0^3(\varepsilon_1 - \varepsilon_0)\sigma \cfrac{1}{\pi^2 n^2}(-1)^{n-1}}{-4T_0^3(\varepsilon_1 - \varepsilon_0)\sigma \cfrac{1}{\pi n}(-1)^{n-1}}$$

$$\pm \cfrac{\sqrt{\begin{array}{l}\cfrac{T_0^3(\varepsilon_1 - \varepsilon_0)\sigma}{8} + T_0^3(\varepsilon_1 - \varepsilon_0)\sigma 8T_0^3\varepsilon_0 + 16T_0^6\varepsilon_0^2 + \lambda(T)t_w T_0^3(\varepsilon_1 - \varepsilon_0)\sigma k_n^2 \\ + 4\lambda(T)t_w T_0^3\varepsilon_0 k_n^2 + \cfrac{\lambda^2(T)t_w^2 k_n^4}{4} + \cfrac{T_0^6(\varepsilon_1 - \varepsilon_0)^2\sigma^2(-1)^{2n-2}}{4\pi^4 n^4}\end{array}}}{-4T_0^3(\varepsilon_1 - \varepsilon_0)\sigma \cfrac{1}{\pi n}(-1)^{n-1}}$$

$$\cfrac{\sqrt{+\cfrac{T_0^3(\varepsilon_1 - \varepsilon_0)\sigma(-1)^{n-1}}{2\pi^2 n^2}\left(8T_0^3\varepsilon_0 + \lambda(T)t_w k_n^2 + 16\left(Q(T)(\alpha_1 - \alpha_0) - 10(\varepsilon_1 - \varepsilon_0)\sigma T_0^4\right) - 62T_0^3(\varepsilon_1 - \varepsilon_0)\sigma\right)}}{-4T_0^3(\varepsilon_1 - \varepsilon_0)\sigma \cfrac{1}{\pi n}(-1)^{n-1}}$$

This is the exact expression for the Fourier coefficient. For y, the same result is obtained. These t_n can be used in Equation A.11 to calculate ΔT.

REFERENCES

1. Fair Richard B. (1993). Rapid Thermal Processing – A Justification. Rapid. Thermal Processing Science and Technology. Academic Press, Inc.

2. Hebb J. P., Klavs Jensen (1996) The Effect of Multilayer Patterns on Temperture Uniformity during Rapid Thermal Processing, Journal of the Electrochemical Society. Vol. 143, No. 3, pp. 1142 – 1151.

3. Meschede D. (2002) Gerthsen Physik. (21st Edition) Springer Verlag.

4. Kekac S., Yener, Y (1985) Heat Conduction. (2nd Edition), Hemisphere Publishing Corporation.

5. Roozboom Fred. (1993) Manufactruring Equipment Issues in Rapid Thermal. Processing. Rapid Thermal Processing Science and Technology. Academic Press, Inc.

6. Lojek B. (1993) Issues in Manufacturing Equipment Issues in Rapid Thermal Processing. Rapid Thermal Processing Science and Technology. Academic Press, Inc.

7. Kakoschke R., Is there a way to a perfect rapid thermal processing system? Materials Research Society Proceedings, Volume 224, pp. 159-170 (1991).

8. Retrieved August, 2005 from the World Wide Web: http://www2.egr.uh.edu/~smotamar/RTP/RTP.html.

9. Fiory A. T., Ravindra N. M. (2005) Film Emissivity Patterns in Rapid Thermal Processing of Silicon Wafers. TMS Symposium 2005.

10. Retrieved from the World Wide Web: http://www.axcelis.com/.

11. Hisham Z., Massoud, (1993) Rapid Thermal and Processing of Dielectrics Rapid Thermal Processing Science and Technology. Academic Press, Inc.

12. Retrieved from the World Wide Web: http://www.appliedmaterials.com/.

13. Retrieved August, 2005 from the World Wide Web: http://ece-www.colorado.edu/~bart/book/eband5.htm.

14. Ravindra N. M. (2004) Lecture Notes "Physics of Materials", Fall Term 2004.

15. Retrieved August, 2005 from the World Wide Web: http://www.vortek.com/fundamentals.html.

16. Hebb J. P., Klavs J. F. (1997) Multi-Rad User Manual. MIT, Cambridge.

17. Niess J., Berger R., Timans P. J., Nenyei Z. (2002) Pattern Effects and How to Explore Them. 10th International Conference on Advanced Thermal Processing of Semiconductors. RTP 2002.

18. Retrieved August, 2005 from the World Wide Web: http://www.rpi.edu/dept/cieem/mcrusers/tools/wetbench/www/Wafer_Cleaning_Procedures.htm.

19. Vandenabeele P., Maex K., De Keersmaecker R. (1989) Impact of Patterned Layers on Temperature Non-uniformity during Rapid Thermal Processing for VLSI-Applications. Mat. Res. Soc. Symp. Vol. 146., pp. 149 – 160.

20. Nguyen L. H., Dietl W., Niess J., Nenyei Z. Logic in RTP. IEEE RTP'99 Conference Proceedings, pp. 26-38 (1999).

21. Kersch A. (1997) Benefits and Limitations of Radiatively Heated Susceptors. Rapid Thermal and Integrated Processing VI. Materials Research Society Symposium Proceedings Vol. 470 pp. 159 – 173.